Atmos. Chem. Phys., 15, 2489–2518, 2015
www.atmos-chem-phys.net/15/2489/2015/
doi:10.5194/acp-15-2489-2015

Atmospheric Chemistry and Physics
Open Access

A comprehensive laboratory study on the immersion freezing behavior of illite NX particles: a comparison of 17 ice nucleation measurement techniques

N. Hiranuma[1], S. Augustin-Bauditz[2], H. Bingemer[3], C. Budke[4], J. Curtius[3], A. Danielczok[3], K. Diehl[5], K. Dreischmeier[4], M. Ebert[6], F. Frank[3], N. Hoffmann[1], K. Kandler[6], A. Kiselev[1], T. Koop[4], T. Leisner[1], O. Möhler[1], B. Nillius[3,*], A. Peckhaus[1], D. Rose[3], S. Weinbruch[6], H. Wex[2], Y. Boose[7], P. J. DeMott[8], J. D. Hader[9], T. C. J. Hill[8], Z. A. Kanji[7], G. Kulkarni[10], E. J. T. Levin[8], C. S. McCluskey[8], M. Murakami[11], B. J. Murray[12], D. Niedermeier[2,], M. D. Petters[9], D. O'Sullivan[12], A. Saito[11], G. P. Schill[13], T. Tajiri[11], M. A. Tolbert[13], A. Welti[7], T. F. Whale[12], T. P. Wright[9], and K. Yamashita[11,***]**

[1]Institute for Meteorology and Climate Research – Atmospheric Aerosol Research, Karlsruhe Institute of Technology, Karlsruhe, Germany
[2]Leibniz Institute for Tropospheric Research, Leipzig, Germany
[3]Institute for Atmospheric and Environmental Science, Goethe University of Frankfurt, Frankfurt, Germany
[4]Faculty of Chemistry, Bielefeld University, Bielefeld, Germany
[5]Institute for Atmospheric Physics, University of Mainz, Mainz, Germany
[6]Institute of Applied Geosciences, Technical University Darmstadt, Darmstadt, Germany
[7]Institute for Atmosphere and Climate Science, ETH, Zurich, Switzerland
[8]Department of Atmospheric Science, Colorado State University, Fort Collins, CO, USA
[9]Department of Marine Earth and Atmospheric Sciences, North Carolina State University, Raleigh, NC, USA
[10]Atmospheric Science and Global Change Division, Pacific Northwest National Laboratory, Richland, WA, USA
[11]Meteorological Research Institute (MRI), Tsukuba, Japan
[12]Institute for Climate and Atmospheric Science, School of Earth and Environment, University of Leeds, Leeds, UK
[13]Cooperative Institute for Research in Environmental Sciences and Department of Chemistry and Biochemistry, University of Colorado, Boulder, CO, USA
[*]now at: Max-Planck-Institut für Chemie, Mainz, Germany
[**]now at: Department of Physics, Michigan Technological University, Houghton, MI, USA
[***]now at: Snow and Ice Research Center, Nagaoka, Japan

Correspondence to: N. Hiranuma (seong.moon@kit.edu)

Received: 19 August 2014 – Published in Atmos. Chem. Phys. Discuss.: 28 August 2014
Revised: 24 December 2014 – Accepted: 27 January 2015 – Published: 6 March 2015

Abstract. Immersion freezing is the most relevant heterogeneous ice nucleation mechanism through which ice crystals are formed in mixed-phase clouds. In recent years, an increasing number of laboratory experiments utilizing a variety of instruments have examined immersion freezing activity of atmospherically relevant ice-nucleating particles. However, an intercomparison of these laboratory results is a difficult task because investigators have used different ice nucleation (IN) measurement methods to produce these results. A remaining challenge is to explore the sensitivity and accuracy of these techniques and to understand how the IN results are potentially influenced or biased by experimental parameters associated with these techniques.

Within the framework of INUIT (Ice Nuclei Research Unit), we distributed an illite-rich sample (illite NX) as a representative surrogate for atmospheric mineral dust particles to investigators to perform immersion freezing experiments using different IN measurement methods and to obtain

IN data as a function of particle concentration, temperature (T), cooling rate and nucleation time. A total of 17 measurement methods were involved in the data intercomparison. Experiments with seven instruments started with the test sample pre-suspended in water before cooling, while 10 other instruments employed water vapor condensation onto dry-dispersed particles followed by immersion freezing. The resulting comprehensive immersion freezing data set was evaluated using the ice nucleation active surface-site density, n_s, to develop a representative $n_s(T)$ spectrum that spans a wide temperature range ($-37\,°C < T < -11\,°C$) and covers 9 orders of magnitude in n_s.

In general, the 17 immersion freezing measurement techniques deviate, within a range of about 8 °C in terms of temperature, by 3 orders of magnitude with respect to n_s. In addition, we show evidence that the immersion freezing efficiency expressed in n_s of illite NX particles is relatively independent of droplet size, particle mass in suspension, particle size and cooling rate during freezing. A strong temperature dependence and weak time and size dependence of the immersion freezing efficiency of illite-rich clay mineral particles enabled the n_s parameterization solely as a function of temperature. We also characterized the $n_s(T)$ spectra and identified a section with a steep slope between −20 and −27 °C, where a large fraction of active sites of our test dust may trigger immersion freezing. This slope was followed by a region with a gentler slope at temperatures below −27 °C. While the agreement between different instruments was reasonable below ∼ −27 °C, there seemed to be a different trend in the temperature-dependent ice nucleation activity from the suspension and dry-dispersed particle measurements for this mineral dust, in particular at higher temperatures. For instance, the ice nucleation activity expressed in n_s was smaller for the average of the wet suspended samples and higher for the average of the dry-dispersed aerosol samples between about −27 and −18 °C. Only instruments making measurements with wet suspended samples were able to measure ice nucleation above −18 °C. A possible explanation for the deviation between −27 and −18 °C is discussed. Multiple exponential distribution fits in both linear and log space for both specific surface area-based $n_s(T)$ and geometric surface area-based $n_s(T)$ are provided. These new fits, constrained by using identical reference samples, will help to compare IN measurement methods that are not included in the present study and IN data from future IN instruments.

1 Introduction

1.1 Background

Primary ice formation by atmospheric ice-nucleating particles (INPs) markedly influences the formation and life cycle of mixed-phase clouds and very often also initiates precipitation formation. Therefore, ice-containing clouds play a significant role in the energy balance of the climate system and the hydrological cycle on Earth (Chapter 7 of IPCC 2013; Boucher et al., 2013). Currently, quantitative predictions for the impact of these clouds on the Earth's radiative budget and thereby the climate are highly uncertain. This uncertainty arises primarily from a lack of fundamental understanding of ice microphysical processes, the representation of these processes in cloud models and knowledge of the abundance of INPs (Hoose and Möhler, 2012; Murray et al., 2012). In particular, yearly emission rates of soil dust are 1000 to 4000 teragrams, accounting for a major proportion of both the dust component and the total particle loading in the atmosphere (Boucher et al., 2013). The resulting radiative forcing directly exerted by mineral dust is estimated to range from -0.3 to $+0.1\,W\,m^{-2}$. Therefore, dust slightly contributes to the direct cooling effect of aerosols. However, our understanding of the influence of the dust burden upon overall climate forcing, including its secondary effect on cloud albedo, remains highly uncertain, in part due to the absence of accurate INP representations in atmospheric models. Thus, the effective radiative forcing effect of airborne dust on current climate predictions remains unresolved.

A small subset of all particles acts as INPs across a range of subzero temperatures, triggering ice formation in clouds via the process of heterogeneous ice nucleation. Previous laboratory experiments have taken diverse approaches in an attempt to mimic ice nucleation and freezing processes. These heterogeneous ice formation processes include deposition nucleation, immersion freezing, condensation freezing, and contact freezing (Vali, 1985), inside-out contact freezing (i.e., freezing of an immersed INP in contact with the droplet surface from the inside; Durant and Shaw, 2005; Fornea et al., 2009) and surface condensation freezing (i.e., freezing of supercooled water or residual aqueous solution trapped on particle surfaces, e.g., by the inverse Kelvin effect; Christenson, 2013; Hiranuma et al., 2014a; Marcolli, 2014; Welti et al., 2014; Wex et al., 2014). Without INPs, pure cloud water droplets or solution within particles can be supercooled to below −37 °C before freezing (Koop et al., 2000; Murray et al., 2010; Rosenfeld and Woodley, 2000).

Among the various modes of atmospheric ice nucleation, immersion freezing is one of the most important mechanisms for primary ice formation, accounting for 85 % of ice formation in clouds that contain supercooled droplets (Hoose et al., 2010). Furthermore, many of the previous experimental studies have investigated heterogeneous ice nucleation at conditions where water is supercooled before freezing (e.g., Murray et al., 2012). However, the relative importance of the particles' physicochemical properties (i.e., size, composition, solubility, hygroscopicity, cloud condensation nuclei (CCN) activity, ice nucleation (IN) active sites, surface charge and/or crystallographic structure) for immersion freezing is not yet well known (e.g., Hiranuma et al., 2013, 2014b; Murray et al., 2012). Hence, more in-depth

investigations and understanding of heterogeneous ice nucleation processes in supercooled clouds (as well as mixed-phase clouds) is of particular importance.

1.2 State of the art of IN measurement techniques

The concept of condensation nuclei contributing to ice formation was first introduced by Alfred Wegener in 1911 (Wegener, 1911). Since then, various instruments and methods have been developed to investigate the composition of atmospherically relevant INPs as well as their abundance; for example, the rapid expansion cloud-simulation chamber (RECC) was first introduced as a detector of ionizing particles. Such instruments have been used in many ice nucleation studies since the 1940s (e.g., Cwilong, 1947; Fournier d'Albe, 1949; Palmer, 1949; Bigg, 1957; Kline and Brier, 1961). Supersaturated conditions with respect to water and ice, as a function of temperature, are created in the RECC vessel by a rapid pressure drop caused by mechanical expansion and concomitant cooling. Subsequently, water vapor in the supersaturated air can either deposit or condense on sample particles, leading to the formation of water droplets and/or ice.

A different type of instrument widely used to measure abundance and efficiency of INPs is the continuous flow diffusion chamber (CFDC). The need for portable instruments capable of obtaining continuous measurements for aircraft applications emerged in discussions during the 1970s was a main driver of CFDC development. In CFDCs, particles are sampled into a region between two ice-coated concentric cylinders (or dual parallel plates) maintained at different temperatures, which generates a region of ice supersaturation between ice-coated walls. As the particles experience ice supersaturation conditions for a few seconds, INPs can be activated and diffusively grow to supermicron ice crystals. Typically, these large ice crystals can be detected and counted by an optical particle counter (OPC) downstream of the instrument while the chamber temperature and humidity conditions are continuously recorded. Since its first appearance in the 1980s with horizontal parallel plates (Hussain and Saunders, 1984; Tomlinson and Fukuta, 1985), several new designs and operational principles have been introduced (e.g., vertically oriented cylinders; Rogers et al., 1988, horizontally oriented parallel plates; Kanji and Abbatt, 2009, vertically oriented parallel plates; Stetzer et al., 2008; Chou et al., 2011; Friedman et al., 2011). An alternative configuration is the continuous flow mixing chamber (e.g., Fast Ice Nucleus Chamber or FINCH; Bundke et al., 2008). The operation principle of this type of chamber does not involve water vapor diffusion from the ice walls, as in CFDC, but water vapor is available for ice growth from the humidified air within the chamber flow. This leads to an upper limit on INP concentrations that are observable with this methodology (DeMott et al., 2011). A flow tube (e.g., Leipzig Aerosol Cloud Interaction Simulator or LACIS, Hartmann et al., 2011) has also been developed in which a humidified stream containing aerosol particles is first cooled to activate droplets on the particles, which upon further cooling may then freeze.

In addition to chamber techniques, the mode-specific conditions for heterogeneous ice nucleation of a known INP placed on a substrate surface have been studied using optical microscope techniques. For example, by immersing ice nuclei in water droplets placed on a hydrophobic substrate surface and collecting a series of images at controlled cooling rates, the change in reflectivity and opacity following ice formation can be characterized, and the associated freezing conditions can be identified (e.g., Knopf and Alpert, 2013; Murray et al., 2011). More recently, other optical microscopy techniques coupled with a unique method of encapsulating particles into droplets followed by cooling (Iannone et al., 2011) or using the hydrophobic squalene/water emulsion (Wright and Petters, 2013) were introduced to the community. Using a similar approach, substrate-supported cooling studies have been applied to determine the freezing temperature in the contact mode (e.g., Fornea et al., 2009; Niehaus et al., 2014), or of deposition nucleation (e.g., Kanji and Abbatt, 2006; Bingemer et al., 2012; Dymarska et al., 2006). The microscopy-coupled substrate-supported freezing devices are advantageous for visualizing the consequences of specific ice nucleation modes in controlled and simulated environments. In some studies, immersion freezing of microliter scale droplet volumes was analyzed at temperatures (Ts) higher than $-10\,^{\circ}\mathrm{C}$ with a sensitivity of INP concentration as good as $\sim 10^{-5}\,\mathrm{L}^{-1}$ (Ardon-Dreyer et al., 2011).

The freezing temperature of INPs either immersed in or in contact with levitated supercooled water droplets suspended in the air can also be determined by the change in light scattering with a charge-coupled device (CCD) camera using an electrodynamic balance (EDB; Hoffmann et al., 2013), an acoustic levitator (Diehl et al., 2014) or in a vertical wind tunnel (Szakáll et al., 2009). The advantage of these methods is the ability to provide, via high-resolution images, substrate-free information for statistically representative ice nucleation processes on a single droplet basis. This advantage is shared with all of the above-mentioned chamber and flow tube devices.

Undoubtedly, these enormous efforts to develop numerous IN measurement techniques have advanced our basic knowledge of atmospheric ice formation. As a consequence, the atmospheric science community will continue to pursue investigations of IN to unravel their associated effects on climate. Accordingly, exploring the sensitivities, uncertainties and biases of various experimental techniques (e.g., methods for particle generation, size segregation, size estimation, ice detection and any other notable experimental procedures) in nucleating ice on particles of known physicochemical properties is crucial in order to compile comparative INP data of multiple and complex measurement techniques from various research institutions. The information obtained from one technique guides other measurement techniques (DeMott et

al., 2011; Riechers et al., 2013). A better understanding of the sensitivity of multiple techniques and the role of associated experimental parameters upon INP measurements will also help in transferring the laboratory-based measurements of INPs of various atmospheric constituents to their reliable parameterizations in models of atmospheric processes.

Since the 1960s, four international workshops have been organized to compare the performance of IN measuring instruments that were emerging or available at the time (DeMott et al., 2011). In particular, effort was made during the fourth international ice nucleation workshop in 2007 (ICIS-2007) to assemble a total of nine laboratory and field IN instruments at the AIDA (Aerosol Interaction and Dynamics in the Atmosphere) facility and compare them using identical test dust samples (e.g., Arizona Test Dust, or ATD, and Saharan dust) over similar thermodynamic conditions. State-of-the-art knowledge was obtained from each workshop activity, and such measurement understanding was further incorporated to develop the next generation of IN instruments.

1.3 Objectives

The major aim of this study, and concurrent studies within the framework of the INUIT (Ice Nuclei Research Unit) project, is to investigate the immersion freezing behavior of reference particles (e.g., Snomax for bacterial IN processes and potassium-rich feldspar, K-feldspar, for mineral dust IN processes). In this work, we distributed illite NX samples from the same batch [with the exceptions of the samples used for Leeds-NIPI, ZINC and IMCA-ZINC (acronyms are defined in the Supplement Sect. S4); Broadley et al., 2012; Welti et al., 2009] among the INUIT project and associated partners. With a total of 17 different IN measuring instruments, we intercompared IN data from each instrument in order to obtain a comprehensive data set for evaluating immersion freezing properties of illite NX particles. The data set captures the functional dependence of various experimental parameter variables, such as particle concentration, particle size, droplet size, temperature, cooling rate and nucleation time, on the immersion freezing properties of illite NX particles. Further, some instruments used test samples suspended in water prior to experiments, while others used dry-dispersed particles. The basic experimental methods and parameterization approaches used to interpret the overall results and perform the intercomparison are discussed.

Results of freezing efficiencies at specific temperatures are presented using the ice nucleation active surface-site density (n_s) parameterization (e.g., Connolly et al., 2009; Niemand et al., 2012; Hoose and Möhler, 2012) developed on the basis of suggestions by DeMott et al. (1995). For instance, Niemand et al. (2012) showed that the singular parameterization approach of immersion freezing (i.e., freezing along water saturation conditions while cooling) of various desert dust particles derived from AIDA experiments converge upon one representative fit as a function of temperature, which is valid across a temperature range from -12 to $-36\,^{\circ}\mathrm{C}$. The time-independent n_s parameterization has also been used in describing INP activation by several different constituents of clay minerals, e.g., microcline and kaolinite, using the cold stage droplet freezing technique (Atkinson et al., 2013; Murray et al., 2010, 2011). Hence, comparison of IN efficiencies can be readily performed for multiple types of instruments using n_s parameterizations. Moreover, such time-independent and surface-area-scaled n_s formulations can be further adapted to comprehensively assess ice nucleation in a wide range of atmospherically relevant temperatures and relative humidities with respect to ice (RH_{ice}), as was recently presented in Hiranuma et al. (2014a). The n_s parameterization for both immersion freezing and deposition nucleation can be directly implemented in cloud, weather and climate models to calculate the temperature-dependent abundance of INPs as a function of the aerosol surface area concentration.

2 Methods

2.1 Illite NX characterization

In this study, we have chosen illite NX (Arginotec, NX Nanopowder) as a surrogate for natural desert dusts. This choice of an illite-rich material is based on a comparison of its mineralogical composition to that of desert dusts, which are also rich in illite but are also mixed with a range of other minerals (Broadley et al., 2012). The present work gives an overview of laboratory experiments for immersion freezing of particles of illite NX, used as a surrogate for atmospheric desert dust particles. Illite NX bulk powder was previously characterized for its physicochemical properties, such as mineralogy and specific surface area (SSA or θ for brevity). It was observed that illite NX samples contained more than 74 weight percent (wt %) illite (Broadley et al., 2012; Friedrich et al., 2008) along with other components [kaolinite, quartz, calcite and feldspars (most likely orthoclase/sanidine), see Sect. 3.1 for more detail] which is similar to the X-ray diffraction (XRD) data specified by the manufacturer. These test particles typically have aggregates of many nanometer-sized grains, yielding an order of magnitude greater SSA ($104.2\,\mathrm{m^2\,g^{-1}}$; Broadley et al., 2012). The aspherical and elongated nature of illite NX particles (aspect ratio up to ~ 4.8; Veghte and Freedman, 2014) emphasizes the importance of considering its irregular shape. The manufacturer reports the particle density, after mechanical granulation, as $2.65\,\mathrm{g\,cm^{-3}}$.

To determine the purity of our sample, and to compare this with previous observations, the dust mineralogy of a bulk illite NX sample was characterized using XRD (Waseda et al., 2011) prior to distribution. In addition, complementary energy dispersive X-ray (EDX) spectroscopy analysis was performed to characterize the elemental composition of in-

dividual particles. The illite NX particles were sampled directly from the AIDA chamber using a 47 mm Nuclepore® filter (Whatman, 0.2 µm pore-size, filter Cat. No. 111106) and used in the EDX analysis.

The N_2-adsorption-based SSA (or BET surface, Brunauer et al., 1938) of the illite NX sample was also measured. BET is a gas adsorption technique where the quantity of various gases required to form a monolayer over the entire available surface of dry particles, including internal surfaces, is measured (Gregg and Sing, 1982; Bickmore et al., 2002). From the knowledge of the size of a molecule on the surface, it is possible to determine the total surface area (S_{total}). In this work, BET surface areas were determined using two different gas adsorbates: N_2 and H_2O (resulting in θ_{N_2} and θ_{H_2O}), with the latter being the surface area exposed to water. BET measurements with H_2O were limited to 28 % relative humidity with respect to water (RH_w) to correctly account for a monolayer of H_2O (Quantachrome Instruments, 2013).

The effect of particle processing, such as removal of hydrophilic ions by water, in a water suspension was examined by ion chromatography (IC). The influence of dust washing and discharge of soluble materials on IN propensity has been previously proposed (Welti et al., 2014). More specifically, the authors postulated two different scenarios at different temperatures based on their observations. At temperatures below ~ -38 °C, the washed dust component may have enhanced water condensation below water saturation, and a formed liquid layer presumably may have stabilized the subcritical ice embryo entrapped inside the liquid. The authors proposed this capillary condensation process as a part of condensation freezing or homogeneous nucleation based on the previous observation (Christenson, 2013) and the theoretical framework (Marcolli, 2014). Above ~ -38 °C, on the other hand, heterogeneous nucleation might have been suppressed because the liquid layer derived from the deliquescence of soluble impurities from individual particles may have diminished accessibility of water vapor to active sites (e.g., localized surface features such as cracks and edges), originally proposed by Koehler et al. (2010), preventing the ice embryo formation. In this study, suspended samples were prepared by stirring illite NX powders (0.1 g in 10 mL of 18.2 MΩ cm nanopure water) over 3 weeks. IC (Dionex DX-500 IC System equipped with Dionex CD20 Conductivity Detector) was used to determine the concentrations of washed out cations (K^+, Ca^{2+} and Mg^{2+}) as a function of time. A weak solution of sulfuric acid [5 mL H_2SO_4 (96 wt %) diluted in 2 L of Nanopure water] was used as the eluent. The measurements were conducted in three series: every 5 to 10 s (seconds) within the first 2 min (minutes) (ultra-short time series, USTS), then every 10 min within the first hour after immersion (short time series, STS) followed by a long time series (LTS) with cation concentration measurements conducted every 2 days thereafter for a 3-week period.

2.2 Particle size distribution

Size distributions and the S_{total} (in $\text{m}^2\,\text{cm}^{-3}$) of both suspended and dry-dispersed illite NX particles were characterized using four size measurement techniques (i.e., aerosol size spectrometers and light scattering instruments). In particular, the dynamic light scattering (DLS) size of suspended illite NX particles (0.05 to 1 mg bulk illite NX sample in 1 mL of double-distilled water) was determined using the StabiSizer® (Microtrac Europe GmbH, PMX 200CS) over the range of 0.0008 to 6.5 µm hydrodynamic diameter. A more detailed description of this instrument and its application for studying the size of particles in suspension are addressed in Hiranuma et al. (2014b), and only a brief discussion is given here. The DLS measurements were carried out with negligible contribution of multiple scattering due to the utilized 180° backscattering mode. The hydrodynamic diameter, which was comparable to the volume equivalent diameter, is determined using a refractive index of 1.55 to 1.58 for illite and of 1.333 for water, and a viscosity of water of 1.002 and 0.797 mPa s at 20 and 30 °C, respectively. From this metric, the surface area was calculated assuming spherical particles.

Size distributions of dry polydisperse illite NX particles were measured at AIDA controlled expansion cloud-simulation chamber (CECC) and Meteorological Research Institute (MRI) dynamic CECC (DCECC) prior to the expansion experiments. For AIDA-CECC, de-agglomerated illite NX particles from a rotating brush disperser (PALAS, RGB 1000) were passed through a series of inertial cyclone impactor stages ($D_{50} \sim 1$ and 5 µm) and introduced to the 84 m^3 volume AIDA vessel. Subsequently, a scanning mobility particle sizer (SMPS, TSI Inc., Model 3081 differential mobility analyzer, DMA, and Model 3010 condensation particle counter, CPC) and an aerodynamic particle sizer (APS, TSI Inc., Model 3321) were used to measure particle size distributions over the range of 0.01 to 15.4 µm volume equivalent diameter. The assumption of particle sphericity, a dynamic shape factor (DSF or χ in equations) of 1.49 ± 0.12 (average of 10 measurements $\pm$ standard deviation) and a particle density of 2.65 $\text{g}\,\text{cm}^{-3}$ were used to obtain the geometric-based (volume equivalent) diameter from an APS (Hiranuma et al., 2014b). At MRI-DCECC, a combination of an SMPS (TSI Inc., Model 3936) and a welas® optical particle counter (welas-OPC, PALAS, Sensor series 2500) was used to acquire a size distribution for the size range of 0.01 to 47.2 µm volume equivalent diameter directly from the 1.4 m^3 volume vessel. The same disperser type was used at both chambers for particle generation, and the upstream cyclone impactors ($D_{50} \sim 1$ and 2.5 µm) were similarly deployed to filter out any larger particles and safeguard against injecting these particles into the vessel. We note that a linear correction factor of ~ 2 was applied to convert the optical diameter measured by the welas-OPC to the APS-inferred volume equivalent di-

ameter in several studies (Wagner et al., 2011; Hiranuma et al., 2014a).

The particle number size distribution of dry particles in the 0.3–10 µm diameter range was also measured by a TSI 3330 optical particle sizer (OPS, TSI Inc.; TSI-OPS hereafter). For particle generation, the illite NX sample was dispersed using a magnetic stirrer in a 100 mL glass vessel that was purged with 200 mL min^{-1} of dry particle-free compressed laboratory air, and then diluted further in two stages by approximately 1 : 100 with dry air. Subsequently, the backward scattering intensity of scattered light from a particle illuminated by a laser ($\lambda = 660$ nm) was measured. The instrument estimated the particle size distribution, assuming spherical particles, using Mie theory. As a result, the reported size is a volume equivalent spherical diameter. Additionally, these dry-dispersed particles were used for the immersion mode experiments of FRIDGE as described in the supplementary methods.

2.3 Ice nucleation measurements

The ice nucleation measurement techniques contributing to this collaborative effort are listed in Table 1. Descriptions of each measurement technique and their acronyms are available in Sect. S4. Briefly, four CFDC-type instruments, one continuous flow mixing chamber, two cloud simulation chambers, one diffusion cell, two levitators, one vertical wind tunnel, one laminar flow tube and five cold stage-type systems were employed in the intercomparison. As seen in Table 1, measurement techniques with the first seven instruments (i.e., ID 1 to 7) and the immersion mode measurements of FRIDGE (ID 12) examined droplets produced from bulk illite NX samples in suspension, while the rest used dry-dispersed illite NX powder, sometimes followed by size selection with a DMA. Methods working with suspensions and those using dry particles employed different ways to determine the particle surface area, and the influence of these differences on the determination of n_s was investigated. For instance, CSU-IS was used to investigate the freezing activity of both bulk suspension and size-segregated particles in suspension. Two cloud expansion chambers, AIDA-CECC and MRI-DCECC, examined both polydisperse and size-selected dry illite NX particles. LACIS and IMCA-ZINC measured immersion freezing of droplets, where each droplet contained a single particle, and examined differently sized dry particles. The role of IN modes upon the estimation of n_s was also examined across various temperature ranges. The EDB-based method was used to measure the contact and immersion mode efficiencies of size segregated dry illite NX particles around −30 °C. Immersion freezing results from IMCA-ZINC were compared to previously reported ZINC data (Welti et al., 2009) at temperatures below −31 °C and to PINC data for temperatures below −26 °C. In the present study, we derived ZINC's n_s values from the results reported in Welti et al. (2009). Specifically, ice formation above 105 % $\mathrm{RH_w}$ up to the water drop survival line was used to calculate n_s based on given illite NX particle sizes. We note that the latent heat of condensation has minimal impact on droplet temperature, such that $\mathrm{RH_w} > 105$ % maintains a water supersaturating condition for droplet freezing.

FRIDGE investigated ice nucleation of both dry-dispersed particles on a substrate at fixed temperatures ($-25\,^{\circ}\mathrm{C} < T < -18\,^{\circ}\mathrm{C}$) with increasing humidity ("default" deposition mode nucleation) as well as immersed particles. In the case of immersion freezing experiments with suspended samples, the cell temperature was lowered by 1 °C min^{-1}.

The range of mass concentrations of the bulk illite NX sample in suspension varied from 3.1×10^{-6} wt % (CSU-IS) to 2.6 wt % (M-WT). For dry-dispersed particle measurements, particle concentrations varied from $\sim 10\,\mathrm{cm}^{-3}$ (AIDA) up to $\sim 9000\,\mathrm{cm}^{-3}$ (MRI-DCECC). Experiments with M-AL, M-WT, EDB, and IMCA-ZINC were performed on a single drop basis. The shortest residence time of roughly 1.6 s was used for the laminar flow tube, LACIS, and the slowest cooling rate of 0.3 °C min^{-1} (time-average cooling rate over an expansion, which translates to the equivalent updraft rate of $\sim 0.5\,\mathrm{m\,s}^{-1}$) was used in AIDA-CECC. Altogether, immersion freezing was examined across the temperature range from ∼ −10 to ∼ −38 °C, and over a varied range of cooling rates, nucleation times and particle concentrations (summarized in publically accessible data base available at http://imk-aaf-s1.imk-aaf.kit.edu/inuit/).

2.4 Ice nucleation parameterization

We now describe a method to parameterize surface area-scaled immersion freezing activities using the size equivalent ice nucleation active surface-site density based on geometric size ($n_{s,geo}$; Connolly et al., 2009; Niemand et al., 2012; Hoose and Möhler, 2012). In short, this surface-site density approach approximates ice crystal formation observed in an experiment as a function of temperature, thus not accounting for time dependence. Accordingly, $n_{s,geo}$ can be expressed by

$$n_{s,geo}(T) = -\ln\left(1 - \frac{N_{ice}(T)}{N_{total}}\right)\left(\frac{1}{S_{ve}}\right), \quad (1)$$

in which N_{ice} is the number concentration of formed ice crystals (cm^{-3}), N_{total} is the total number concentration of particles prior to any freezing event (cm^{-3}), and S_{ve} is the volume equivalent surface area of an individual particle (m^2). As demonstrated in Niemand et al. (2012), if the activated ice fraction is small (< 0.1), the Taylor series approximation can be applied to Eq. (1). Assuming a uniform distribution of $n_{s,geo}$ over a given S_{total} and a size independency of $n_{s,geo}$, we can approximate $n_{s,geo}$ as

$$n_{s,geo}(T) \approx \frac{N_{ice}(T)}{N_{total} S_{ve}} = \frac{N_{ice}(T)}{S_{total}}. \quad (2)$$

Table 1. Summary of INUIT measurement techniques and instruments. All acronyms are available in Sect. S4. Note "poly" and "mono" denote polydisperse and quasi-monodisperse size-selected particle distributions, respectively.

ID	Instrument	Description	Portable ?	Reference	Investigable T range	Ice detected T range for this study
1	BINARY*	Cold stage-supported droplet assay	No	Budke and Koop (2015)	$-25\,^{\circ}\mathrm{C} < T < \sim 0\,^{\circ}\mathrm{C}$	$-24\,^{\circ}\mathrm{C} < T < -15\,^{\circ}\mathrm{C}$
2	CSU-IS	Immersion mode ice spectrometer	Yes	Hill et al. (2014)	$-30\,^{\circ}\mathrm{C} < T < \sim 0\,^{\circ}\mathrm{C}$	poly: $-25\,^{\circ}\mathrm{C} < T < -11\,^{\circ}\mathrm{C}$ mono: $-26\,^{\circ}\mathrm{C} < T < -20\,^{\circ}\mathrm{C}$
3	Leeds-NIPI	Nucleation by immersed particles instrument	No	O'Sullivan et al. (2014)	$-36\,^{\circ}\mathrm{C} < T < \sim 0\,^{\circ}\mathrm{C}$	$-21\,^{\circ}\mathrm{C} < T < -11\,^{\circ}\mathrm{C}$
4	M-AL*	Acoustic droplet levitator	No	Diehl et al. (2014)	$-30\,^{\circ}\mathrm{C} < T < \sim 0\,^{\circ}\mathrm{C}$	$-25\,^{\circ}\mathrm{C} < T < -15\,^{\circ}\mathrm{C}$
5	M-WT*	Vertical wind tunnel	No	Szakáll et al. (2009); Diehl et al. (2011)	$-30\,^{\circ}\mathrm{C} < T < \sim 0\,^{\circ}\mathrm{C}$	$-21\,^{\circ}\mathrm{C} < T < -19\,^{\circ}\mathrm{C}$
6	NC State-CS	Cold stage-supported droplet assay	No	Wright and Petters (2013)	$-40\,^{\circ}\mathrm{C} < T < \sim 0\,^{\circ}\mathrm{C}$	$-34\,^{\circ}\mathrm{C} < T < -14\,^{\circ}\mathrm{C}$
7	CU-RMCS	Cold stage-supported droplet assay	No	Schill and Tolbert (2013)	$-40\,^{\circ}\mathrm{C} < T < -20\,^{\circ}\mathrm{C}$	$-32\,^{\circ}\mathrm{C} < T < -23\,^{\circ}\mathrm{C}$
8	AIDA*	CECC	No	Möhler et al. (2003) Hiranuma et al. (2014a, b)	$-100\,^{\circ}\mathrm{C} < T < -5\,^{\circ}\mathrm{C}$	poly: $-35\,^{\circ}\mathrm{C} < T < -27\,^{\circ}\mathrm{C}$ mono: $-34\,^{\circ}\mathrm{C} < T < -28\,^{\circ}\mathrm{C}$
9	CSU-CFDC	Cylindrical plates CFDC	Yes	Tobo et al. (2013)	$-34\,^{\circ}\mathrm{C} < T < -9\,^{\circ}\mathrm{C}$	$-29\,^{\circ}\mathrm{C} < T < -22\,^{\circ}\mathrm{C}$
10	EDB*	Electrodynamic balance levitator	No	Hoffmann et al. (2013)	$-40\,^{\circ}\mathrm{C} < T < -1\,^{\circ}\mathrm{C}$	imm.[a]: $-31\,^{\circ}\mathrm{C} < T < -28\,^{\circ}\mathrm{C}$ contact[b]: $-34\,^{\circ}\mathrm{C} < T < -27\,^{\circ}\mathrm{C}$
11	FINCH*	Continuous flow mixing chamber	Yes	Bundke et al. (2008)	$-60\,^{\circ}\mathrm{C} < T < -2\,^{\circ}\mathrm{C}$	$-27\,^{\circ}\mathrm{C} < T < -22\,^{\circ}\mathrm{C}$
12	FRIDGE*	Substrate-supported diffusion and condensation/immersion cell	Yes	Bingemer et al. (2012)	$-25\,^{\circ}\mathrm{C} < T < -8\,^{\circ}\mathrm{C}$	default[c]: $-25\,^{\circ}\mathrm{C} < T < -18\,^{\circ}\mathrm{C}$ imm.[d]: $-25\,^{\circ}\mathrm{C} < T < -18\,^{\circ}\mathrm{C}$
13	LACIS*	Laminar flow tube	No	Hartmann et al. (2011); Wex et al. (2014)	$-40\,^{\circ}\mathrm{C} < T < -5\,^{\circ}\mathrm{C}$	$-37\,^{\circ}\mathrm{C} < T < -31\,^{\circ}\mathrm{C}$
14	MRI-DCECC	Dynamic CECC	No	Tajiri et al. (2013)	$-100\,^{\circ}\mathrm{C} < T < \sim 0\,^{\circ}\mathrm{C}$	poly: $-26\,^{\circ}\mathrm{C} < T < -21\,^{\circ}\mathrm{C}$ mono: $-29\,^{\circ}\mathrm{C} < T < -21\,^{\circ}\mathrm{C}$
15	PINC	Parallel plates CFDC	Yes	Chou et al. (2011); Kanji et al. (2013)	$-40\,^{\circ}\mathrm{C} < T < -9\,^{\circ}\mathrm{C}$	$-35\,^{\circ}\mathrm{C} < T < -26\,^{\circ}\mathrm{C}$
16	PNNL-CIC	Parallel plates CFDC	Yes	Friedman et al. (2011)	$-55\,^{\circ}\mathrm{C} < T < -15\,^{\circ}\mathrm{C}$	$-35\,^{\circ}\mathrm{C} < T < -27\,^{\circ}\mathrm{C}$
17	IMCA-ZINC	Parallel plates CFDC	No	Lüönd et al. (2010) Stetzer et al. (2008); Welti et al. (2009)	$-65\,^{\circ}\mathrm{C} < T < -5\,^{\circ}\mathrm{C}$	imm.[e]: $-36\,^{\circ}\mathrm{C} < T < -31\,^{\circ}\mathrm{C}$ ZINC[f]: $-33\,^{\circ}\mathrm{C} < T < -32\,^{\circ}\mathrm{C}$

* Instruments of INUIT project partners, [a] immersion freezing, [b] contact freezing, [c] default deposition nucleation, [d] immersion freezing with suspended particles, [e] immersion freezing with IMCA, [f] ZINC alone.

In addition, the IN efficiency can be related to the BET-SSA to estimate BET-inferred ice nucleation surface-site density, $n_{\mathrm{s,BET}}$. A description of the procedures used to estimate both n_{s} metrics is given in Hiranuma et al. (2014b). The advantage of using $n_{\mathrm{s,geo}}$ is its applicability to both measurements and modeling activities due to the assumption of particle sphericity. Conversely, $n_{\mathrm{s,geo}}$ cannot be directly obtained through suspension experiments because the size distribution of a suspended sample for each experiment is not available; therefore, S_{total} is determined from BET and the sample mass suspended in water.

In order to convert $n_{\mathrm{s,geo}}$ values of all dry-dispersed particle measurements into $n_{\mathrm{s,BET}}$, the geometric size-based ice-nucleating mass, $n_{\mathrm{m,geo}}$ (g^{-1}), is first calculated from the IN active surface using either the surface-to-mass conversion factor ($\mathrm{in\,m^2\,g^{-1}}$) of $6/D_{\mathrm{ve}}\rho$ (size-selected case) or $S_{\mathrm{total}}/M_{\mathrm{total}}$ (polydisperse case) by

$$n_{\mathrm{m,geo}}(T) = \frac{N_{\mathrm{ice}}(T)}{N_{\mathrm{total}} M_{\mathrm{ve}}} = \frac{6}{D_{\mathrm{ve}}\rho} n_{\mathrm{s,geo}}(T) \approx \left(\frac{S_{\mathrm{total}}}{M_{\mathrm{total}}}\right) n_{\mathrm{s,geo}}(T), \quad (3)$$

where M_{ve} is the mass of a spherical particle of volume-equivalent diameter (g), D_{ve} is the volume equivalent mid-point diameter of particles (m), ρ is the particle density of illite NX ($2.65 \times 10^6\,\mathrm{g\,m^{-3}}$), and M_{total} is the total particle mass concentration ($\mathrm{g\,cm^{-3}}$). We note that the DLS size distribution-derived $S_{\mathrm{total}}/M_{\mathrm{total}}$ (i.e., DLS-SSA) is $6.54\,\mathrm{m^2\,g^{-1}}$ and use for the measurements with suspended particles. We also note that the conversion factor ranges from 11.3 to $2.26\,\mathrm{m^2\,g^{-1}}$ for size-selected particle diameters from 200 to 1000 nm, respectively, where these sizes denote the range of particle diameters used in the size-selected cases in the present study. Therefore, ice-nucleating mass can be scaled to the BET-SSA (θ, $124.4\,\mathrm{m^2\,g^{-1}}$) to derive $n_{\mathrm{s,BET}}$ as

$$n_{\mathrm{s,BET}}(T) = \frac{n_{\mathrm{m,geo}}(T)}{\theta} \approx \frac{n_{\mathrm{m,sus}}(T)}{\theta} = \frac{\alpha}{M_{\mathrm{ve}}\theta}, \quad (4)$$

in which $n_{\mathrm{m,sus}}$ is the IN active mass for suspension measurements, α represents the ice activated fraction ($= N_{\mathrm{ice}}/N_{\mathrm{total}}$), which is the direct measurement of suspension experiments and some of the dry-dispersed particle methods. With an assumption of a uniform BET-SSA, the resulting $n_{\mathrm{s,BET}}$ may be representative of measurements with suspended samples because minimal corrections (only α and θ) are involved when compared to that with dry-dispersed particles. Owing to internal surface area and surface roughness, BET-SSA may be greater than DLS-SSA (O'Sullivan et al., 2014).

Alternatively, we can also convert ice-nucleating mass derived from suspension measurements, $n_{\mathrm{m,sus}}$, to $n_{\mathrm{s,geo}}$ using DLS-SSA to provide a reasonable comparison to dry-dispersed particle measurements. However, this process re-

quires one more step than when using $n_{s,BET}$ (with an additional assumption of constant size distribution for all suspensions) and two more steps than when using n_m. For our intercomparison study, we used both $n_{s,BET}$ and $n_{s,geo}$. Because fewer conversion factors are involved, $n_{s,BET}$ may be best suited for suspension measurements, and $n_{s,geo}$ may be best suited for dry-dispersed particle measurements (Eq. 3 to 4 or vice versa).

The usage of DLS-SSA for the calculation of S_{total}/M_{total} of suspension measurements appears to be reasonable, as this leads to $n_{s,geo}$ for suspension measurements nearly equivalent to $n_{s,geo}$ for dry-dispersed particles. When S_{total}/M_{total} is derived based on TSI-OPS measurements, a value of $0.49\,m^2\,g^{-1}$ is obtained, which is smaller by a factor of about 13 compared to DLS-SSA. This difference may be mainly due to the fact that dry-dispersed particles are typically prone to agglomeration (discussed below, i.e., Sect. 3.1) compared to the measurements with suspended particles. The presence of fewer agglomerates in suspended particles is shown in Fig. 1 of Hiranuma et al. (2014b). Since the size distribution of a suspended sample for each experiment was not measured, DLS-SSA was used for the data evaluation for suspension measurements throughout this study.

3 Results

3.1 Illite NX characterization

XRD results from the present and previous studies (Friedrich et al., 2008; Broadley et al., 2012) of the major minerals in bulk samples of illite NX are presented in Table 2. The results show that the bulk illite NX powder is composed of various minerals: illite, kaolinite, quartz, calcite and feldspar, but the relative mass of these minerals for this study differs from previous studies. For example, our measurement shows that the illite NX sample is composed of ∼ 69 wt % illite mineral, whereas others report a larger amount of illite from 74 to 86 wt %. Similarly, we observed a somewhat different content of other minerals compared to previous studies as listed in Table 2 (see also the Supplement Fig. S1). We note that the fractional values in compositional fingerprints may deviate even within the same batch, as all three XRD measurements deviated from the manufacturer's data (Table 2). Furthermore, our XRD result indicates that the illite NX sample contains a smaller quartz fraction (3 %) than illite IMt1 from the Clay Minerals Society (10 to 15 % quartz according to the official XRF data and 20 % based on our own measurements).

To complement bulk XRD analysis, the abundances of 13 elements (Pt, K, C, Ca, O, Fe, Mg, Al, Si, P, S, Pb and Ti), which are commonly identified in illite-rich samples, were measured by EDX spectroscopy on a single particle basis. Four representative EDX spectra are presented in Fig. 1. The presence of Fe and Mg is typical and characteristic for illite NX particles. The observed large amounts of Si and Al are due to the presence of layered aluminosilicate structures (i.e., layer of SiO_2 and Al_2O_3). The observed dominant platinum (Pt) signals in all spectra originate from the sputter coating conducted prior to EDX analyses. Figure 1a shows the typical illite spectrum, which is similar to the one previously published in Welton (1984). Illite-rich minerals, which included impurities of calcite, TiO_2 and Pb-P, were located by the brightness difference in the backscattered electron detector micrograph images. The results are shown in Fig. 1b,

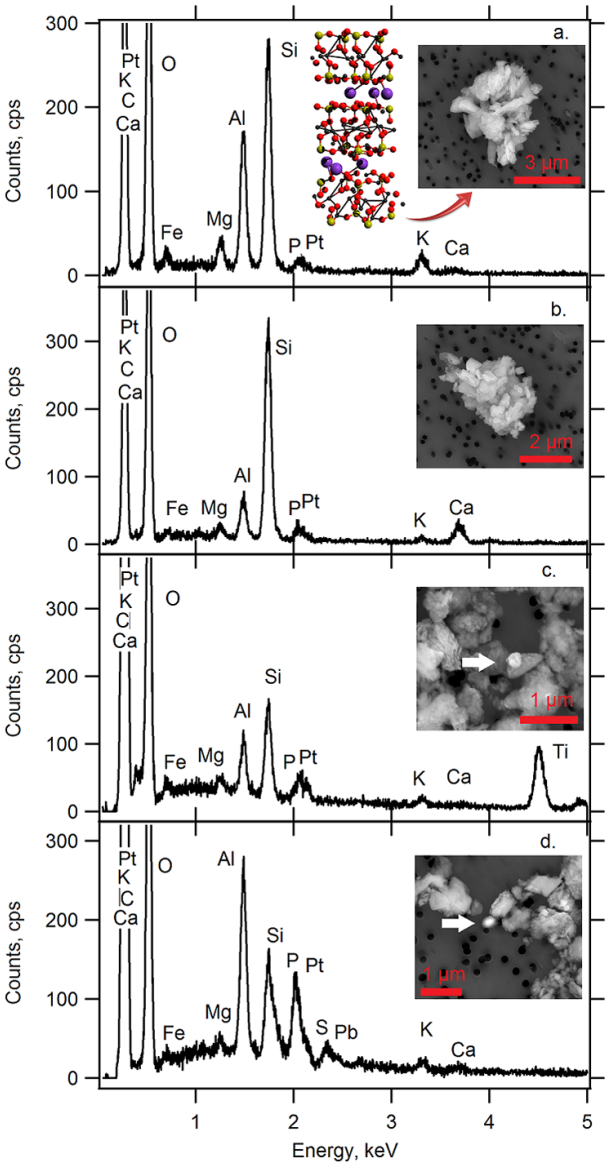

Figure 1. EDX spectra of representative illite NX particles. **(a)** Typical illite, **(b)** calcite-rich mineral, **(c)** titanium-oxide-rich mineral, and **(d)** lead-rich mineral. Scanning electron microscopy images of characterized particles are shown in subpanels. A schematic representation of the illite's crystal structure (silicon in yellow, aluminum in black, oxygen in red and potassium in purple) is also shown.

Table 2. X-ray diffraction analyses of the bulk composition of illite NX powder.

Mineral	Weight Percentage (wt %)			
	This study	Manufacturer Data	Broadley et al. (2012)	Friedrich et al. (2008)*
Illite	69	86	74	76
Kaolinite	10	10	7	5
Quartz	3	4	7	< 1
Calcite/Carbonate	3	N/A	2	2
Feldspar (Orthoclase/Sanidine)	14	N/A	10	4

* Friedrich et al. (2008) noted 11 wt % additional impurities, including phlogopite (7.8 wt %), anhydrite (1.4 wt %), plagioclase (1.1 wt %), and apatite (0.7 wt %).

c and d (inclusion of calcite, TiO_2 and Pb-P, respectively). However, the EDX technique is not automated to detect these impurities present within the illite NX particles because of their very small weight fraction. Therefore, the possible effect of these observed impurities in illite NX upon the ice nucleation activity cannot be evaluated on the basis of its bulk analysis of the chemical composition. Nonetheless, detection of non-illite mineral components may reflect the complexities of natural dust particles, which typically contain multiple sites with differing nucleation abilities. Thus, illite-rich clay minerals can be used as reference material to mimic the ice nucleation activity of physically and chemically complex natural dusts (Murray et al., 2012).

The measured BET-SSA are 124.4 and 123.7 $m^2\,g^{-1}$ with N_2 and H_2O vapor, respectively, as the adsorbing gas on illite NX particle surfaces. The similar BET surface areas for both N_2 and H_2O vapor gas adsorption suggest that the formation of a few monolayers of H_2O does not alter the surface morphology or the mineralogical phase of illite NX particles. For comparison, our measurements of θ_{N_2} for illite NX particles agreed with previously reported data within 20 % (104.2 $m^2\,g^{-1}$; Broadley et al., 2012). Since illite NX particles have significant internal surface area, BET-derived surface areas can be expected to be larger than those derived from the laser diffraction technique. Supporting this notion, an SEM (scanning electron microscopy) image of an illite NX particle from Broadley et al. (2012) shows how micron-sized particles are made up of many nanometer-sized grains.

Normalized surface area distributions to the total surface area concentration measured by four different techniques are shown in Fig. 2. According to the manufacturer, 95 % (by mass) of the dry and mechanically de-agglomerated illite NX particles have a diameter smaller than 650 nm (i.e., D_{95}). This mass-based particle size is substantially smaller than that of another type of Arginotec illite (Arginotec, SE-illite, $D_{95} = 5\,\mu m$). Interestingly, all mass size distributions measured in this study (not shown here) indicate a substantial mass fraction above 650 nm which is, in all cases, larger than 5 % (18, 24, 77 and 99.9 % for DLS, AIDA, MRI-DCECC and TSI-OPS for the FRIDGE immersion experiments, respectively), indicating the presence of agglomerates in the aerosol and suspension phases prepared for the IN experiments. The surface area distribution of the DLS hydrodynamic diameter-based measurement (Fig. 2a) agreed well with in situ measurements from the AIDA chamber (Fig. 2b), suggesting the size distributions of dry illite NX

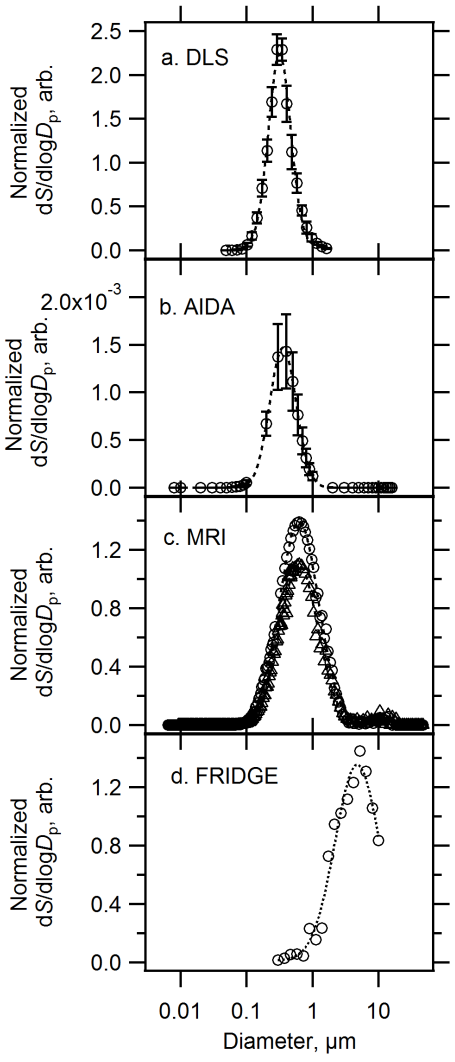

Figure 2. Surface area distributions of **(a)** suspended and **(b–d)** dry illite NX particles. Hydrodynamic size-based surface area distributions are measured in suspension using DLS. The average (± standard error) of five measurements with different concentrations of suspended illite NX powder (0.05, 0.1, 0.25, 0.5 and 1 mg mL^{-1}) is presented in **(a)**. Volume equivalent diameter-based dry-dispersed particle surface area distributions measured in the AIDA chamber (mean of 10 measurements ± standard error) and MRI-DCECC (two individual measurements) are shown in **(b)** and **(c)**, respectively. Panel **(d)** shows optical diameter-based particle surface area distributions measured by a TSI-OPS used for the FRIDGE immersion mode experiments. Dotted lines represent log-normal fittings, and corresponding mode diameters are **(a)** 0.32 µm, **(b)** 0.36 µm, **(c)** 0.62 µm and **(d)** 4.75 µm. The width-parameters of log-normal fittings are **(a)** 0.55, **(b)** 0.65, **(c)** 0.95 and **(d)** 1.10.

particles during AIDA experiments were similar to those of suspension measurements. This observation is consistent with results presented in Hiranuma et al. (2014b). Briefly, the authors found agreement between the DLS-based hydrodynamic diameter and the AIDA-derived volume equivalent diameter of hematite particles. As opposed to the AIDA observation, the wider distributions and the shift in the mode diameters in the MRI-DCECC measurements towards a larger size (0.62 µm, Fig. 2c) when compared to Fig. 2a and b may indicate a higher degree of particle agglomeration as a result of different degrees of pulverization during the particle generation processes or particle coagulation at the high aerosol number concentration used for these measurements. A more pronounced agglomeration effect was observed by the TSI-OPS measurements (Fig. 2d), such that a surface area distribution of supermicron-sized particles was obtained. Thus, different types of dry particle dispersion methods can contribute to varying degrees of agglomeration and the observed differences in surface area distributions. Though all size segregating instruments used in the present study are well calibrated, we cannot rule out the effect of measurement techniques themselves on the observed differences in particle size distribution. In Sect. 4.4 we discuss whether agglomeration has an effect on the IN activity.

The cation release by illite NX in the aqueous suspension was measured with IC as a function of time. The suspension was kept mechanically agitated for 3 weeks. The following cations were identified in the samples: K^+, Ca^{2+} and Mg^{2+}. As seen in Fig. 3, IC data clearly demonstrates that roughly all cations were released into the aqueous environment by illite NX almost instantaneously. The concentration of the cations increased rapidly and reached equilibrium within the first 2 min after immersion of sample into water. Of all the cations measured, only Ca^{2+} exhibited a slow concentration raise on the longer time scales.

3.2 Immersion freezing measurements and intercomparisons

All ice nucleation spectra with $n_{s,BET}(T)$ and $n_{s,geo}(T)$ are shown in Figs. 4 and 5, respectively. A similar figure with $n_m(T)$ is also shown in Fig. S2. Furthermore, we compare the n_s data from 17 instruments to 4 literature results. Specifically, IN spectra reference curves of previously reported illite NX particles (Broadley et al., 2012, hereafter B12), microcline particles (Atkinson et al., 2013, hereafter A13), ATD and desert dusts (Niemand et al., 2012, hereafter N12) are also expressed as both $n_{s,BET}(T)$ and $n_{s,geo}(T)$. The conversion between $n_{s,geo}(T)$ and $n_{s,BET}(T)$ was performed according to (Eqs. 3 and 4). The $n_s(T)$ (m^{-2} as a function of °C) fits from the reference literature are

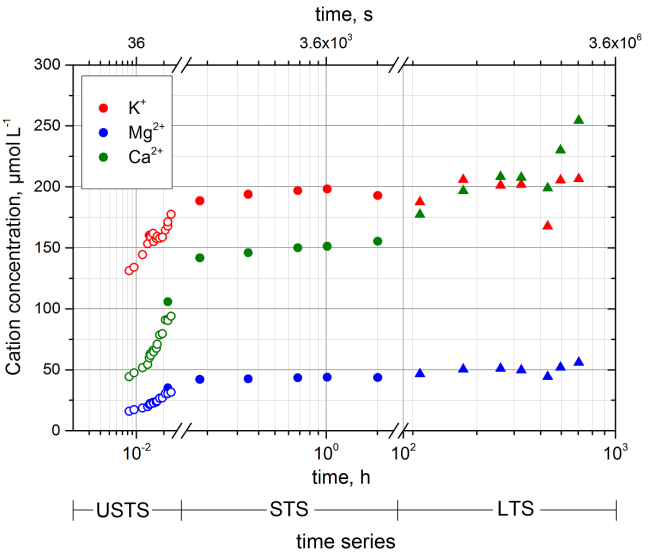

Figure 3. Evolution of the cation concentration in aqueous suspension of 0.1 g illite in 10 mL deionized water with time. The scaling of the time-axis is different for three different subsections of the time series (USTS, STS and LTS).

$$n_{s,BET}^{A13} = 10^4 \times \exp(-1.038\,(T + 273.150) + 275.260), \quad (5)$$

$$n_{s,BET}^{B12} = 10^4 \times \exp\Big[\Big(6.530 \times 10^4\Big) + \Big(\Big(-8.215 \times 10^2\Big) \times (T + 273.150)\Big) + \Big(3.447 \times (T + 273.150)^2\Big) + \Big(\Big(-4.822 \times 10^{-3}\Big) \times (T + 273.150)^3\Big)\Big], \quad (6)$$

$$n_{s,geo}^{N12(ATD)} = \exp(-0.380T + 13.918), \quad (7)$$

$$n_{s,geo}^{N12(Dust)} = \exp(-0.517T + 8.934). \quad (8)$$

For microcline (K-feldspar), the $n_{s,geo}$ to $n_{s,BET}$ conversion was performed using a laser diffraction-based surface-to-mass conversion factor of 0.89 $m^2\,g^{-1}$ and an N_2 BET-SSA of 3.2 $m^2\,g^{-1}$ (Atkinson et al., 2013). For ATD and natural dust, we used a surface-to-mass conversion factor of 3.6 $m^2\,g^{-1}$, assuming a monodisperse particle size at the log-normal fit mode diameter of 0.64 µm (Niemand et al., 2012) and the measured N_2 BET-SSA of 34.4 $m^2\,g^{-1}$ (this study). We note that the ATD parameterization is valid only for $-26.7\,°C < T < -17.7\,°C$. In addition, we also present 14, 0.14 and 0.0014 % scaled A13 $n_s$curves to see if K-feldspar (microcline) can be used as a scaling factor to determine the $n_s(T)$ of illite NX.

We do not attempt to completely discuss the immersion freezing activity of illite NX particles measured by each measurement technique. Instead, brief remarks regarding each

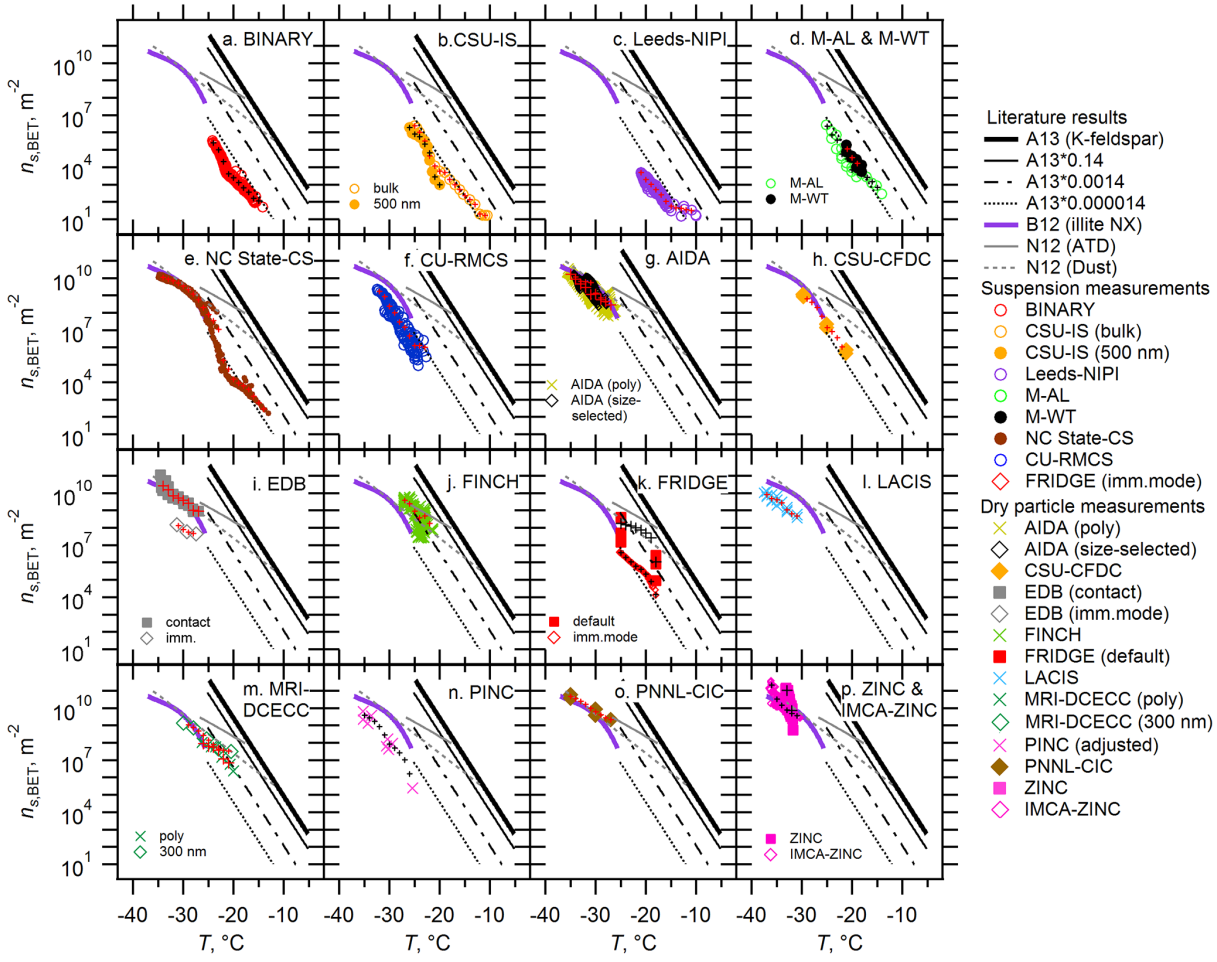

Figure 4. Intercomparison of 17 instruments using $n_{s,BET}$. Black or red cross markers are interpolated $n_s(T)$ used for T-binned averaging. Note that M-AL and M-WT results are presented in **(d)**. In **(k)**, FRIDGE results of default (solid square) and imm.mode (open diamond) measurements are presented. Both ZINC (solid square) and IMCA-ZINC (open diamond) data are shown in **(p)**. Reference immersion freezing $n_s(T)$ spectra for illite NX (B12; Broadley et al., 2012), K-feldspar (A13; Atkinson et al., 2013), ATD and desert dusts (Dust) (N12; Niemand et al., 2012) are also shown (See Sect. 3.2).

method are summarized below. The detailed discussion of the methods intercomparison follows in Sect. 3.3.

3.2.1 BINARY

This recently developed microliter droplet assay technique demonstrated its capability of measuring immersion freezing of clay minerals in the temperature range of -15 to $-24\,°C$. Similar to most of the other suspension-based techniques, BINARY identified a steep $n_s(T)$ increase, which started just below $-20\,°C$. The BINARY $n_s(T)$ spectrum was derived by compiling measurements with varied illite NX mass concentrations over 2 orders of magnitude (0.1 to 10 mg mL^{-1}, see the supplementary methods). Immersion freezing efficiency of illite NX particles collapsed into a single $n_s(T)$ spectrum, i.e., IN efficiency does not depend on suspended particle mass for the concentration range studied here. This observation is a check for consistency and it implies that ice nucleation is indeed triggered by suspended illite NX particles, and neither by impurities contained in the water used for dilution nor at the glass surface supporting the droplets. If IN efficiency did depend on suspended particle mass, different $n_s(T)$ spectra would result from the various illite NX concentrations, which are shifted by the respective dilution factor.

3.2.2 CSU-IS

This new immersion freezing device was used to investigate the freezing activity of both bulk suspension and size-segregated particles in suspension. A new approach was employed for size-selected measurements, wherein 500 nm mobility diameter size-selected particles were collected on a Nuclepore filter and then rinsed from it for the immersion freez-

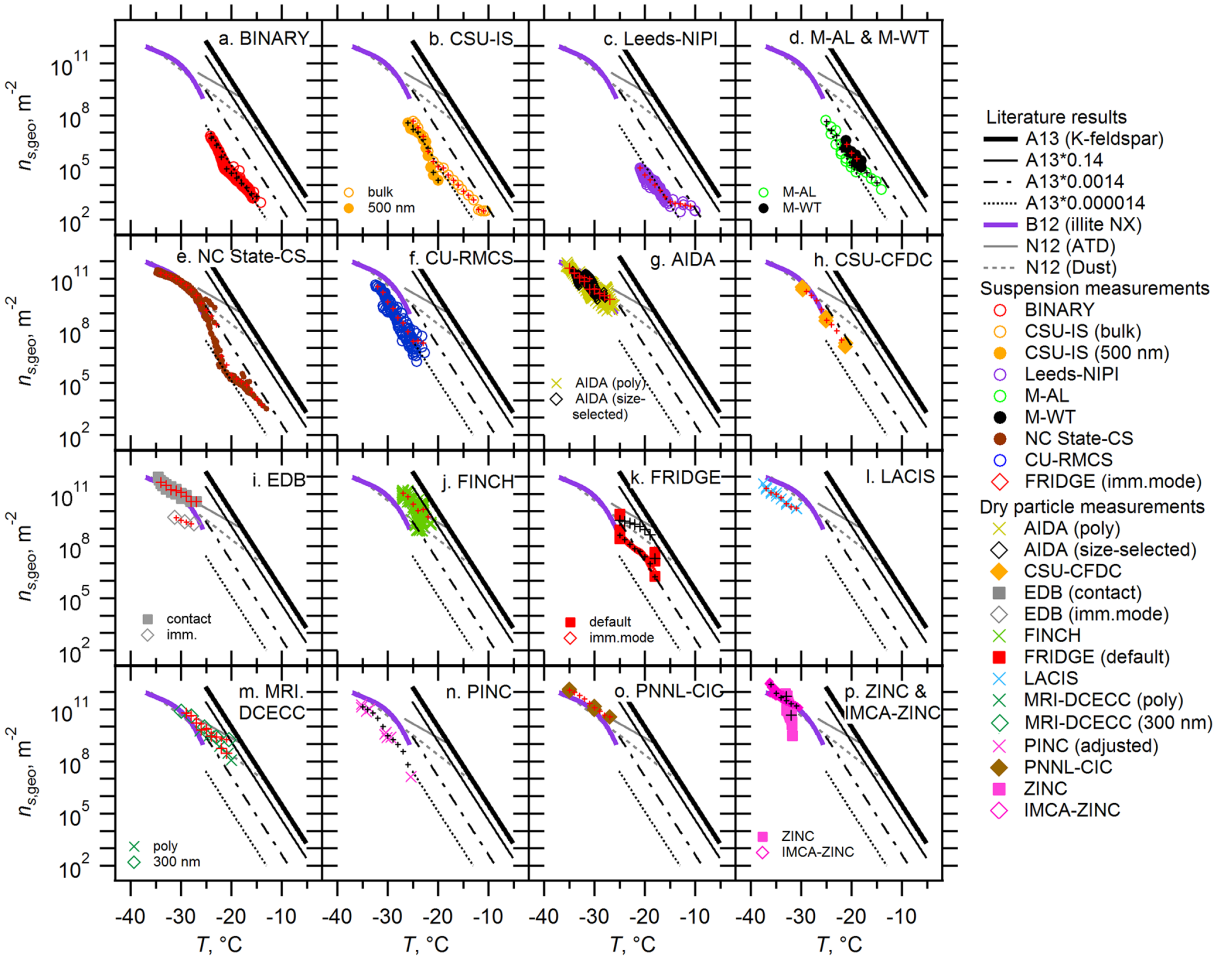

Figure 5. Geometric size-based ice nucleation active surface-site density, $n_{s,geo}$, of 17 measurement techniques. Black or red cross markers are interpolated $n_s(T)$ used for T-binned averaging. Note that M-AL and M-WT results are presented in **(d)**. In **(k)**, FRIDGE results of default (solid square) and imm.mode (open diamond) are presented. Both ZINC (solid square) and IMCA-ZINC (open diamond) data are shown in **(p)**. Reference immersion freezing $n_s(T)$ spectra are provided as in Fig. 4.

ing measurements. The results suggest size independence of n_s within the experimental uncertainties (a combination of binomial sampling error and the uncertainty of conversion of aerodynamic particle diameter to mass) for the range of examined size (500 nm vs. bulk) and mass concentrations of bulk illite NX powder in suspensions from 3.1×10^{-6} to 0.5 wt %, for non-size-segregated particles, and 2.2×10^{-5} to 4.4×10^{-4} wt % for size-segregated particles.

3.2.3 Leeds-NIPI

This suite of cold stage instruments has the capacity to operate using droplets with volumes in the microliter to picoliter range. This enables high resolution immersion freezing analysis for a wide range of temperatures from higher ($-22\,°C < T < -11\,°C$) to lower temperatures ($-37\,°C < T < -26\,°C$). The highest freezing temperatures are attained with the largest droplets, which contain the largest surface area of illite NX. Combined with the previous parameterization reported in Broadley et al. (2012), the Leeds-NIPI data follows the overall $n_s(T)$ spectrum defined by the bulk of the instruments. This suggests that immersion freezing efficiency, inferred by $n_s(T)$, of illite NX particles is dependent on neither droplet volume nor mass of illite NX particles in suspension (i.e., wt % 0.1 or 1 %); instead the freezing efficiency only depends on the surface area per droplet. Together with CSU-IS, these two instruments provided data points for temperature as high as $\sim -11\,°C$, estimating a similar lower-limit of $n_{s,BET}$ values of $\sim 10\,m^{-2}$.

3.2.4 M-AL and M-WT

Both methods examine individual drops that are freely suspended without any contact with walls or substrates. In M-WT drops are floated at their terminal velocities in a laminar air stream, in which conditions of ventilation and heat

transfer are similar to those of droplets falling through the atmosphere. Both M-AL and M-WT techniques analyzed the freezing efficiency of drops containing polydisperse illite NX particles in the temperature range between −14 and −26 °C. The n_s values agree reasonably well with substrate-supported suspension experiments (with the exception of FRIDGE experiments), implying that the surface making contact with the substrate has a negligible effect on immersion freezing for our experimental conditions.

3.2.5 NC State-CS

Extensive experimental conditions were realized by NC State-CS (Wright and Petters, 2013; Hader et al., 2014). Unique aspects of this instrument are the sampling of drops within a squalene oil matrix that allows for experiments using cooling rates as slow as 0.01 K min^{-1} and an automated freeze detection algorithm that allows for the rapid processing of more than 1000 possible drops per experiment to improve sample statistics. Drops containing ∼ 0.0001 to 1.0 wt % of the illite NX test sample were studied at a cooling rate of 1 K min^{-1} to find the immersion freezing ability. A total of nine immersion mode freezing experiments, spanning a range of drop volumes from ∼ 400 picoliter to 150 nanoliter, were performed. Using this instrument a wide range of temperatures was investigated ($-34\,^{\circ}\mathrm{C} < T < -14\,^{\circ}\mathrm{C}$) yielding $n_s(T)$ values ranging from 10^2 to 10^{10} m^{-2}. The data from the nine individual runs collapsed into a single $n_s(T)$ spectrum suggesting that the mass loading of dust in the drop did not affect the measurements for the wt % values investigated. At the high T end ($T > -20\,^{\circ}\mathrm{C}$), the data are in reasonable quantitative agreement with the CSU-IS measurements. At the low T end ($T < -20\,^{\circ}\mathrm{C}$), the data are in agreement with the B12 reference spectrum.

3.2.6 CU-RMCS

The University of Colorado (CU)-RMCS examined the freezing abilities of droplets containing 1.0 wt % illite NX. CU-RMCS detected the warmest immersion freezing of illite NX particles at about −23 °C under the experimental conditions used in the present work (see the Supplement for further details). Results for $-32\,^{\circ}\mathrm{C} < T < -23\,^{\circ}\mathrm{C}$ are from six different experiments using four different droplet size bins: 10–20, 20–60, 60–120, and 120–200 µm (lateral diameter). These droplet sizes correspond to a variation in droplet volume from ∼ 0.3 picoliter to 2.5 nanoliter.

3.2.7 AIDA

The AIDA cloud simulation chamber generates atmospherically relevant droplet sizes (several µm in diameter, varying with cooling rates), and therefore closely simulates mixed-phase cloud conditions. Ice-nucleating efficiencies of both polydisperse and quasi-monodisperse illite NX particles were investigated in this study. n_s of DMA size-selected illite NX particles (200, 300 and 500 nm mobility diameter) agreed well with that of the polydisperse population for immersion freezing experiments, within previously reported uncertainties ($T \pm 0.3$ °C and $n_s \pm 35$ %; Steinke et al., 2011). Thus, a negligible size dependency of n_s for "submicron" dry illite NX particles for temperatures below −27 °C was found. Previously, Hiranuma et al. (2014a) demonstrated the size independence of the n_s value using two different sizes of submicron hematite particles (200 and 1000 nm volume equivalent diameter) based on AIDA deposition mode nucleation experiments. Such a similarity might remain true for the immersion mode freezing of mineral dust particles that are smaller than 1 µm diameter.

3.2.8 CSU-CFDC

This CFDC provided data for condensation/immersion freezing at around −21.2, −25.1 and −29.7 °C (a total of eight data points with two, two and four points at around each temperature, respectively), which extends to a warmer region than the AIDA measurements. As demonstrated in DeMott et al. (2015), higher RH_w values were required for full expression of immersion freezing in CSU-CFDC. The use of 105 % RH_w in the CFDC has been shown to underestimate INP activity for natural dusts by up to a factor of 3, but is a necessary compromise. Comparably, the CSU-CFDC results agreed well with the AIDA measurements within a factor of 3 in $n_{s,geo}$ estimation (AIDA n_s > CSU-CFDC n_s; DeMott et al., 2015). All the CFDC measurements were conducted with 500 nm mobility diameter size-selected particles, as discussed in the supplementary methods.

3.2.9 EDB

With EDB, both the contact and immersion mode freezing efficiencies of illite NX particles were investigated. The contact nucleation mode n_s were clearly higher than the immersion mode n_s (by more than 1 order of magnitude in terms of $n_{s,geo}$, Fig. 5i). This was in part due to the fact that immersion freezing experiments were conducted only when illite NX particles were not frozen via contact nucleation but remained immersed in a supercooled droplet in the EDB cell (see the Supplement).

3.2.10 FINCH

The immersion freezing results from FINCH showed the highest n_s values in the −22 to −27 °C temperature range out of all of the other instrument results. All the FINCH measurements were conducted with 500 nm mobility diameter size-selected particles. Two possible reasons for high n_s values when compared to the other measurements are: (1) an overestimation of $n_s$due to excess N_{ice} and/or underestimated S_{total} or (2) a large temperature-uncertainty. It is noteworthy that the total INP concentration was kept below 140 L^{-1} in order to avoid saturation limitation due to

a high number of growing ice crystals (DeMott et al., 2011). A constant total concentration of particles continuously passing through the chamber was maintained at $1.07 \pm 0.17\,\mathrm{cm}^{-3}$ (average $\pm$ standard deviation).

3.2.11 FRIDGE

FRIDGE data, which cover both measurements of dry and immersed particles with the same instrument but with different sample processing, lie within the upper edge of the bulk of other n_s data points. There are a few important implications from the FRIDGE results. First, on average, the measurements with dry particles in the "default" setting showed more than an order of magnitude higher n_s in comparison to the immersed particles in FRIDGE experiments (both $n_{s,BET}$ and $n_{s,geo}$, Figs. 4 and 5) at $-25\,^{\circ}\mathrm{C} < T < -18\,^{\circ}\mathrm{C}$. For instance, FRIDGE experiments in the pure immersion mode showed much lower n_s than that with the default setting (i.e., combined deposition and immersion mode), but agreed with other immersion data sets. Second, a sudden increase in $n_s(T)$ was found for the measurements with immersed particles at $\sim -20\,^{\circ}\mathrm{C}$, suggesting a dominant activation around $-20\,^{\circ}\mathrm{C}$. This transition is a unique behavior only found with the FRIDGE's IN detecting sensitivity. A temperature shift (i.e., shifting the data $\sim 7\,^{\circ}\mathrm{C}$ lower) results in FRIDGE data overlapping with the bulk of other data and may offset discrepancies. However, other mechanistic interpretations (e.g., contribution of agglomeration) are also plausible causes of this discrepancy. More detailed discussions of the role of agglomerates upon n_s and sample processing are available in Sects. 4.4 and 4.5.

3.2.12 LACIS

With the shortest instrument residence time (~ 1.6 s), LACIS measured immersion mode freezing of illite NX particles for three different mobility diameters (300, 500 and 700 nm) from $-31\,^{\circ}\mathrm{C}$ down to the homogeneous freezing temperature. Similar to AIDA results, a size independence of n_s of submicron illite NX particles was observed within defined experimental uncertainties (see the supplementary methods). Further, without any data corrections, the results of LACIS reasonably agreed with AIDA measurements. Furthermore, though there is no overlapping temperature range for LACIS and CSU-CFDC in the present study, consistency between data from LACIS and CSU-CFDC for other clay minerals (i.e., different kaolinite samples) has been described previously (Wex et al., 2014). The results from both instruments agreed well with each other from a data evaluation based on n_s, and this agreement was even improved when the different residence times in LACIS and the CSU-CFDC were accounted for (i.e., when nucleation rate coefficients were compared). Furthermore, a size independence of the immersion mode freezing was seen for Fluka-kaolinite particles with mobility diameters of 300 and 700 nm in Wex et al. (2014), and for illite NX particles when comparing particles with mobility diameters of 500 nm to bulk material (Augustin-Bauditz et al., 2014).

3.2.13 MRI-DCECC

Comparison between polydisperse and size-selected (300 nm mobility diameter) measurements in this cloud simulation chamber demonstrated the size independency of n_s for submicron illite NX particles for slightly higher temperatures (up to $-21\,^{\circ}\mathrm{C}$) than AIDA results. Interestingly, MRI-DCECC data exhibited at least an order of magnitude higher n_s values than most other suspension measurements. We note that only negligible freezing events were detected above $-21\,^{\circ}\mathrm{C}$ even with a $\sim 9000\,\mathrm{cm}^{-3}$ number concentration of polydisperse illite NX particles in part due to the detection limit of the welas® optical counter of $N_{ice} = 0.1\,\mathrm{cm}^{-3}$.

3.2.14 PINC

PINC provided data for immersion freezing at around -25.4, -30.2 and $-34.6\,^{\circ}\mathrm{C}$ (a total of nine data points with one, four and four points at around each temperature, respectively). The estimated $n_s$values are in agreement with other measurements for the test range of $-35\,^{\circ}\mathrm{C} < T < -25\,^{\circ}\mathrm{C}$ after applying a residence time correction of about a factor of 3. The data are for ice nucleation onto 500 and 1000 nm mobility diameter illite NX particles; therefore, an OPC threshold size of 2 µm for ice detection is used. The impactor used for sampling particles into PINC was characterized for size-resolved particle losses and was found to have a cutoff (D_{50}) of 725 nm mobility diameter. As such, when determining $n_{s,geo}$ the particles losses (25 to 60 %, see the Supplement for more details) were taken into account for calculating activated fractions. We note that $n_{s,geo}$ increased after correcting the data for particle losses, resulting in agreement between the data from PINC and data from LACIS, AIDA and UC-RMCS in the temperature range from -25 to $-35\,^{\circ}\mathrm{C}$.

3.2.15 PNNL-CIC

The IN efficiency of illite NX particles in the immersion mode in the temperature range of $-35\,^{\circ}\mathrm{C} < T < -27\,^{\circ}\mathrm{C}$ was observed to increase at lower temperatures. Estimated n_s values were somewhat higher in this temperature range when compared to those from most of the other measurements. Data were obtained at conditions where PNNL-CIC was operated at 105 % RH_w at three different temperatures. Dust particles greater than ~ 1 µm (50 % cut size) were removed before they were size-selected and transported to the PNNL-CIC. The OPC detection threshold was set ≥ 3 µm; see the Supplement for more details.

3.2.16 IMCA-ZINC

Coupled with IMCA, ZINC showed reasonable agreement with AIDA and PNNL-CIC. This reproducibility verified the performance of the IMCA-ZINC combination, which was not tested during ICIS-2007 (DeMott et al., 2011), perhaps due to the similarity in the experimental conditions (i.e., particle generation) to the other two methods. We also note that the residence time in ZINC is about a factor of 3 longer than that in PINC. The IMCA-ZINC measurements in comparison to the measurements with ZINC alone (i.e., a combination of deposition nucleation, contact freezing, condensation freezing, surface condensation freezing and immersion freezing) is discussed in Sect. 4.5 in more detail.

Overall, as described above (Sects. 3.2.1 to 3.2.6), suspension experiments with cold stage devices and levitation techniques provide IN measurements under more controlled (with respect to droplet size, concentration and mass of particles) conditions and a wider temperature range (up to $-11\,^{\circ}\mathrm{C}$) than comparable dry-dispersed particle experiments. The resulting n_{s}values from these suspension experiments are also independent of the total number of droplets and suspended dust particle mass.

The estimated n_{s}values of dry test particles below $-25.5\,^{\circ}\mathrm{C}$ are in reasonable agreement with a previous study (Broadley et al., 2012) at temperatures below $-25\,^{\circ}\mathrm{C}$. Furthermore, the strong temperature dependence and size independence of n_{s} may suggest a uniform distribution of freezing sites over the total surface of illite NX particles in the immersion mode in this temperature range. Specifically, AIDA and MRI-DCECC have shown size-independent n_{s} values for submicron dry-dispersed particles. Overall, compared to suspension measurements, dry-dispersed particle measurements showed higher n_{s} values. For example, FINCH is the only instrument which showed higher n_{s} values than the parameterization by Niemand et al. (2012) for ATD. Likewise, AIDA results indicated slightly higher n_{s} values than CSU-CFDC's results. The lower n_{s} of CSU-CFDC may be a consequence of underestimation of N_{ice}, possibly due to its constrained $\mathrm{RH_w}$ (at 105 %) and/or the disturbance of aerosol lamina between two plates in a CFDC (DeMott et al., 2015).

3.3 Intercomparisons based on the slope parameter of $n_{\mathrm{s}}(T)$ spectra

A compilation of 17 n_{s} spectra from 17 instruments in a temperature range between -10.1 and $-37.5\,^{\circ}\mathrm{C}$ is presented in Fig. 6. For both the geometric area-based and the BET area-based n_{s}, the differences among measurements can be more than 1 order of magnitude at any given temperature. Diversity is especially pronounced for several orders of magnitude in n_{s} at $-27\,^{\circ}\mathrm{C} \leq T \leq -18\,^{\circ}\mathrm{C}$, where the results from suspension measurements and a majority of dry measurements coexist (see the investigated T range for each technique in Table 1). Another notable feature of this specific temperature range in Fig. 6 is the coincidence of the steepest slope in the spectrum (i.e., the absolute value of $\Delta\log(n_{\mathrm{s}})/\Delta T$ or $|\Delta\log(n_{\mathrm{s}})/\Delta T|$ in $\log(\mathrm{m}^{-2})\,^{\circ}\mathrm{C}^{-1}$, hereafter denoted as $\Delta\log(n_{\mathrm{s}})/\Delta T$) when compared to other temperature ranges. For instance, n_{s} increases sharply at temperatures colder than $-18\,^{\circ}\mathrm{C}$ to be nearly parallel to the A13 parameterization down to $-27\,^{\circ}\mathrm{C}$, where it starts leveling off and is eventually overlapping with the N12 parameterization at the low temperature segment.

Correspondingly, the overall trend of the spectrum is traced by the measurements from NC State-CS alone (Fig. 4e). Moreover, the slopes of the spectrum for three sub-segments ($-34\,^{\circ}\mathrm{C} < T < -27\,^{\circ}\mathrm{C}$, $-27\,^{\circ}\mathrm{C} < T < -20\,^{\circ}\mathrm{C}$, and $-20\,^{\circ}\mathrm{C} < T < -14\,^{\circ}\mathrm{C}$) can be calculated from interpolated data and compared to N12 and A13 parameterizations. As expected, the steepest slope in the spectrum ($= 0.66$) of the NC State-CS data was found in the $-27\,^{\circ}\mathrm{C} < T < -20\,^{\circ}\mathrm{C}$ range, which was similar to that of the A13 parameterization (0.45 for $T > -25\,^{\circ}\mathrm{C}$). However, smaller slope values are found for the other two segments (0.18 for $T < -27\,^{\circ}\mathrm{C}$ and 0.29 for $T > -20\,^{\circ}\mathrm{C}$), which are comparable to the temperature-independent N12 slopes (0.17 for ATD and 0.22 for Dust) and the B12 slope (0.25 for $-35\,^{\circ}\mathrm{C} < T < -27\,^{\circ}\mathrm{C}$), suggesting that a dominant fraction of INP contained in our test dust becomes ice active in immersion freezing at $-27\,^{\circ}\mathrm{C} < T < -20\,^{\circ}\mathrm{C}$. In addition, FRIDGE immersion mode measurements also show a sharp decrease in $\Delta\log(n_{\mathrm{s}})/\Delta T$ (from 0.59 to 0.25, Figs. 4k and 5k) for the measurements with immersed particles at $\sim -20\,^{\circ}\mathrm{C}$. Similar observations are made by most of the other suspension measurement techniques. In short, most suspension methods capture the steepest segment of the $n_{\mathrm{s}}(T)$ spectral slopes ($\Delta\log(n_{\mathrm{s}})/\Delta T$) at $-27\,^{\circ}\mathrm{C} < T < -20\,^{\circ}\mathrm{C}$, where the slope is nearly parallel to the A13 parameterization. One exception is CU-RMCS (Fig. 4f). The highest possible freezing temperature investigated by this experimental system was about $-23\,^{\circ}\mathrm{C}$ with ~ 2.5 nanoliter droplets containing 1.0 wt % illite NX (see the supplementary methods). Hence, CU-RMCS did not capture the transition in $\Delta\log(n_{\mathrm{s,BET}})/\Delta T$ at around $-20\,^{\circ}\mathrm{C}$, but the steep slope of the spectrum ($= 0.36$) validated the high density of IN active sites below $-23\,^{\circ}\mathrm{C}$. The error in temperature for this technique is always $\pm 0.5\,^{\circ}\mathrm{C}$, based on freezing experiments without any foreign substances in supercooled drops (i.e., homogeneous freezing experiments).

Similarly, dry-dispersed particle measurements also exhibit scattered data for their measured temperature ranges. Both agreements and equally important disagreements were observed. First, the agreements are summarized. AIDA data show that the values of $\Delta\log(n_{\mathrm{s,geo}})/\Delta T$ ($= 0.22$, Fig. 5g) are identical for both polydisperse and size-selected measurements, perhaps suggesting a uniform distribution of active sites over the available S_{total} of illite NX in this study. Similarly, IMCA-ZINC's $\Delta\log(n_{\mathrm{s,geo}})/\Delta T$ ($= 0.24$, Fig. 5p) derived from 200, 400 and 800 nm mobility diameters is vir-

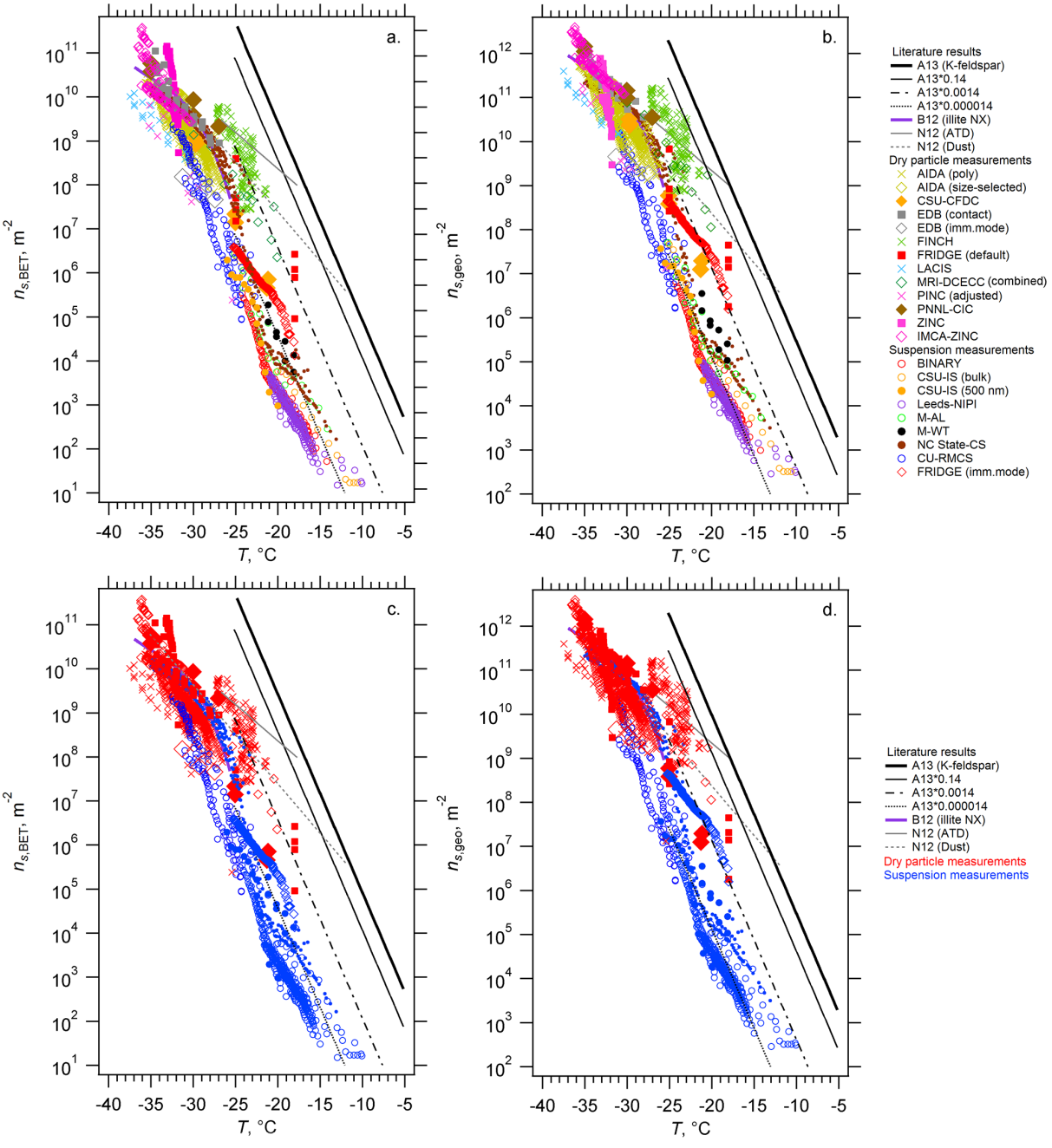

Figure 6. Immersion freezing $n_s(T)$ spectra of illite NX particles from 17 instruments calculated as a function of the BET **(a)** and geometric **(b)** surface areas. Reference immersion freezing $n_s(T)$ spectra are provided as in Figs. 4 and 5. Dry-dispersed particle (red markers) and suspension (blue markers) results for $n_{s,BET}$ and $n_{s,geo}$ are shown in **(c)** and **(d)**, respectively, to highlight the difference between dry particle and suspension subsets.

tually identical to the slope estimated from AIDA measurements. PINC estimated $\Delta\log(n_{s,geo})/\Delta T$ ($=0.26$, Fig. 5n) values are in reasonable agreement with AIDA and IMCA-ZINC and N12 parameterizations at temperatures below $-25\,°C$. From the CSU-CFDC results, $\Delta\log(n_{s,geo})/\Delta T$ derived from interpolated data is 0.40 (Fig. 5h). Considering the AIDA and CSU-CFDC data, the $n_s(T)$ spectrum depicts similar trends (i.e., n_s or temperature deviation around $-27\,°C$) compared to those seen in the NC State-CS results (Fig. 5e) and is also parallel to the A13 curve (slope $=0.45$) down to temperatures around $-27\,°C$ and is parallel to the N12 Dust curve (slope $=0.22$) for the lower temperature segment. LACIS measurements show that $\Delta\log(n_{s,geo})/\Delta T$ ($=0.19$, Fig. 5l) is also in agreement with that from AIDA, verifying

a deteriorated freezing ability of illite NX particles in the investigated temperature range. EDB was used to examine both the contact and immersion freezing modes. Nonetheless, the slopes of the spectra for both modes (0.11 for immersion mode freezing and 0.16 for contact mode freezing, Fig. 5i) are similar to the N12 ATD curve (slope = 0.17). From the fact that the value of $\Delta\log(n_{s,geo})/\Delta T$ of FINCH (= 0.27, Fig. 5j) above −27 °C is similar to that of the N12 dust parameterization (whereas this relationship would be expected below −27 °C), we suspect that a temperature uncertainty may be the main cause of the observed deviation of its data from others. Lastly, at −35 °C < T < −27 °C, PNNL-CIC's $\Delta\log(n_{s,geo})/\Delta T$ (= 0.19, Fig. 5o) agreed well with that of the N12 dust parameterization in the same temperature range.

Next, the disagreements between dry-dispersed particle and suspension measurements are discussed. Specifically, the MRI-DCECC results show lower values of $\Delta\log(n_{s,geo})/\Delta T$ (= 0.29) up to −21 °C as compared to the suspension measurements. Additionally, in the temperature range from −29 °C < T < −21 °C, the MRI-DCECC data show higher values of n_s than those observed in suspension measurements. This relatively constant $\Delta\log(n_s)/\Delta T$ value along with higher $n_s$values through the range contrasts with the observed sharp transition in $\Delta\log(n_s)/\Delta T$ in suspension measurements. We note that MRI-DCECC experiments may have been carried out in the presence of a high degree of agglomeration (Fig. 2c and d). Hence, particle processing (i.e., drying and suspension) may not be the only factor causing this difference and other contributions cannot be ruled out (see Sect. 4).

To conclude, the results from suspension and dry measurements suggest evidence that the n_s of illite NX particles derived from immersion freezing is independent of or only weakly dependent on droplet size, mass percent of illite NX sample in suspension and droplets, particle size of the tested illite NX and cooling rate during freezing in the range of conditions probed; see the Supplement for more detailed information regarding experimental conditions for each instrument. Overall, the sample processing (i.e., dry vs. suspension sample) may have an effect on the immersion freezing efficiency of illite clays. A more detailed discussion will follow in Sect. 4 below.

4 Discussion

For detailed comparison of methodologies, the immersion freezing properties of illite NX particles in a wide range of temperatures is further discussed by comparing $n_s(T)$ spectra from all 17 instruments (Sect. 4.1). Specifically, we present T-binned average data (i.e., 1 °C bins for −37 °C < T < −11 °C). A moving average (where original data points are finer than 1 °C) or a Piecewise Cubic Hermite Interpolating Polynomial function (where original data points are coarser than 1 °C) was used for data interpolation. All data from the 17 instruments, as shown in Figs. 4 and 5, were interpolated.

We also discuss potential reasons for the diversity observed from intercomparisons of dry and suspension measurement techniques. Both systematic errors (Sect. 4.2) and mechanistic uncertainties (Sects. 4.3 to 4.6) are qualitatively evaluated to understand the measurement uncertainties of such techniques. Some factors may introduce diversity in n_s, whereas others may shift activation temperatures horizontally to match the n_s values from other instruments, perhaps biasing the overall accuracy and precision of instruments. Here we address the relative importance of those factors with respect to their effect on the estimation of n_s.

4.1 Dry vs. suspension $n_s(T)$ data

The multiple exponential distribution fits (also known as the Gumbel cumulative distribution function) for T-binned-$n_s(T)$ data are shown in Fig. 7. The fits for T-binned maxima and minima n_s from 17 measurement techniques are presented as pink shaded areas. All fits presented in this figure are derived using parameters shown in Table 3. As can be inferred from the table, a higher correlation coefficient (r) was found when intercomparing the suspension measurements as compared with intercomparing the dry-dispersed methods, suggesting reasonable agreement and consistency for the results from immersion freezing studies with suspensions. Interestingly, a higher r for $n_{s,geo}$ than $n_{s,BET}$ was found for dry-dispersed particle measurements as compared to the suspension measurements. The use of more conversion factors to estimate $n_{s,BET}$ (i.e., from Eqs. 3 and 4) may introduce uncertainties and discrepancies between these measurement techniques. It is also noteworthy that the T-binned ensemble maximum and minimum values are largely influenced by dry-dispersed particle and suspension results, respectively, implying the previously discussed discrepancy between these two techniques.

It is observed that the largest deviation between the maxima and minima in the horizontal and vertical axes, corresponding to $\mathrm{Hor}_{\mathrm{Max-Min}}$ and $\mathrm{Ver}_{\mathrm{Max-Min}}$, respectively, shown in Fig. 7, is similar for both $n_{s,BET}$ (Fig. 7a) and $n_{s,geo}$ (Fig. 7b). Nevertheless, $n_{s,BET}$ is representative of measurements with suspended samples because fewer corrections and assumptions are involved for its estimation when compared to that with dry-dispersed particles. Hence, $n_{s,BET}$ may be a good proxy for comparing IN efficiencies of dust particles from various instruments. We also report the absolute values of $\Delta\log(n_s)/\Delta T$ for four T-segregated segments based on T-binned Lin. Avg. (multiple exponential distribution fit to the T-binned average data in the linear space), T-binned Max. (fit to the T-binned maxima in the linear space) and T-binned Min. (fit to the T-binned minima in the linear space) in Fig. 7 (i.e., T_1 to T_4). The slopes are comparable to the slope of the A13 parameterization in the T_1 to T_3 segments (−11 to −27 °C), while the slope in the T_4 segment is

Table 3. List of the Gumbel cumulative distribution fit parameters to the $n_{s,BET}$ and $n_{s,geo}$ for T-binned ensemble data set fitted in the linear space [All (lin)], ensemble data set fitted in the log space [All (log)], ensemble maximum values (All_{max}), ensemble minimum values (All_{min}), suspension subset fitted in the linear space [Sus (lin)], suspension subset fitted in the log space [Sus (log)], dry-dispersed particle subset fitted in the linear space [Dry (lin)] and dry-dispersed particle subset fitted in the log space [Dry (log)]. Note that All_{max} and All_{min} are fitted in the linear space. The correlation coefficient, r, for each fit is also shown. T is in °C.

Fitted data set	Fitted T range	Fit parameters [$n_{s,BET}(T) = \exp(a \cdot \exp(-\exp(b \cdot (T+c)))+d)$]				
		a	b	c	d	r
All (lin)*	$-37\,°C < T < -11\,°C$	23.82	0.16	17.49	1.39	0.60
All (log)*	$-37\,°C < T < -11\,°C$	22.00	0.16	20.07	3.00	0.80
All_{max}*	$-37\,°C < T < -11\,°C$	24.72	0.15	17.27	1.56	0.63
All_{min}*	$-37\,°C < T < -11\,°C$	21.86	0.16	22.73	2.70	0.94
Sus (lin)	$-34\,°C < T < -11\,°C$	24.38	0.14	19.61	1.89	0.99
Sus (log)	$-34\,°C < T < -11\,°C$	24.28	0.14	21.19	2.70	0.99
Dry (lin)*	$-37\,°C < T < -18\,°C$	27.35	0.07	16.48	3.19	0.59
Dry (log)*	$-37\,°C < T < -18\,°C$	26.22	0.07	16.27	3.31	0.72
Fitted data set	Fitted T range	Fit Parameters [$n_{s,geo}(T) = \exp(a \cdot \exp(-\exp(b \cdot (T+c)))+d)$]				
		a	b	c	d	r
All (lin)*	$-37\,°C < T < -11\,°C$	25.75	0.13	17.17	3.34	0.73
All (log)*	$-37\,°C < T < -11\,°C$	22.93	0.16	20.31	5.72	0.80
All_{max}*	$-37\,°C < T < -11\,°C$	25.72	0.15	16.39	3.52	0.75
All_{min}*	$-37\,°C < T < -11\,°C$	22.16	0.16	22.13	5.64	0.98
Sus (lin)	$-34\,°C < T < -11\,°C$	22.72	0.16	19.52	5.50	1.00
Sus (log)	$-34\,°C < T < -11\,°C$	22.64	0.16	20.93	5.92	0.98
Dry (lin)*	$-37\,°C < T < -18\,°C$	29.38	0.05	16.49	7.19	0.64
Dry (log)*	$-37\,°C < T < -18\,°C$	27.92	0.05	13.25	6.32	0.83

* To derive the fits that are representative for immersion mode freezing, we excluded EDB (contact) and ZINC data.

similar to those of the N12 parameterizations. These results are consistent with the results described in Sect. 3.3. Further, $Ver_{Max-Min}$ for roughly 3 orders of magnitude with respect to n_s is observed in a temperature region around $\sim -20\,°C$ for both $n_{s,BET}(T)$ and $n_{s,geo}(T)$ spectra. Such high $n_s$variability was expected due to the contribution from MRI-DCECC, FINCH and FRIDGE measurements, which may have influenced the overall fit in that temperature range. Likewise, our $Hor_{Max-Min}$ shows that the 17 measurements are in reasonable agreement within 7.8 °C (−36.8, −33.0, −29.0 °C (min, log fit, max)) at $n_{s,BET}$ of $5.2 \times 10^9\,m^{-2}$ and 7.5 °C (−36.7, −32.8, −29.2 °C (min, log fit, max)) at $n_{s,geo}$ of $1.5 \times 10^{11}\,m^{-2}$.

T-binned $n_{s,BET}(T)$ and $n_{s,geo}(T)$ spectra are presented in Fig. 8a and b, respectively. In this figure, panels i, ii and iii show T-binned data averaged in the linear space of all 17 instruments, all suspension type measurements, and all measurements that involved dry particles, respectively, while panel iv shows a comparison between suspension and dry-particle measurements. We note that the data from "EDB (contact)" and "ZINC" (Welti et al., 2009) were not used for generating T-binned data since our focus was on immersion mode freezing. We also note that the n_s results from nine IN measurement techniques provide n_s data at −23 and −24 °C, where we find an abrupt increase in $\Delta\log(n_s)/\Delta T$ and n_s deviations. Investigated T ranges for each instrument are listed in Table 1.

As described in Sect. 3.2, suspension measurements possess sensitivity at high temperatures (up to −11 °C), indicating that their ability to control the concentration or dilution of suspension over a wide range is of great advantage in detecting rare INPs. Moreover, suspension experiments with small picoliter or nanoliter droplets allow measurements right down to the homogeneous freezing limit ($\sim -37\,°C$; Koop et al., 2000). In turn, suspension methods with microliter droplets may run into "background problems" at temperatures below about −20 to −25 °C for samples that do not contain many IN active at these temperatures, because then impurities contained in the water may trigger freezing. Conversely, dry aerosol methods lack sensitivity for detecting rare IN at high temperatures because of their low sample volume. These dry particle measurements are in general good for low temperature measurements, where the number of particles nucleating ice increases and instruments

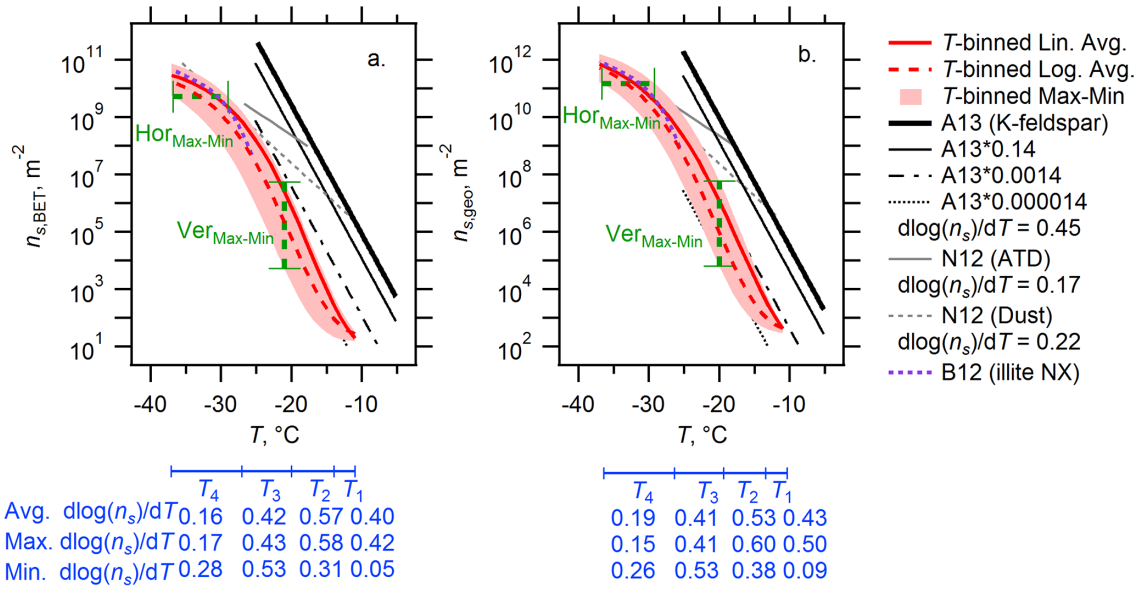

Figure 7. The n_s parameterization, based on the BET **(a)** and geometric **(b)** surface areas, as a function of temperature (T). The multiple exponential distribution fit in the linear space (T-binned Lin. Avg.) is expressed as $n_{s,BET}(T) = \exp(23.82 \times \exp(-\exp(0.16 \times (T + 17.49))) + 1.39)$ or $n_{s,geo}(T) = \exp(25.75 \times \exp(-\exp(0.13 \times (T + 17.17))) + 3.34)$. The same fit in the log space (T-binned Log. Avg.) is expressed as $n_{s,BET}(T) = \exp(22.00 \times \exp(-\exp(0.16 \times (T + 20.07))) + 3.00)$ or $n_{s,geo}(T) = \exp(22.93 \times \exp(-\exp(0.16 \times (T + 20.31))) + 5.72)$. Note that n_s and T are in m^{-2} and °C, respectively. The maximum deviation between maxima and minima in horizontal axis (in T, °C) and vertical axis [in $\log(n_{s,max}/n_{s,min})$] corresponds to Hor$_{Max-Min}$ and Ver$_{Max-Min}$, respectively. All fit parameters are shown in Table 3.

have higher ice detection efficiencies. For temperatures below −27 °C, our T-binned fits exhibit a reasonable agreement with the suspension experiments reported by Broadley et al. (2012). Furthermore, dry-dispersed particle measurements show higher n_s values when compared to suspension measurements above about −27 °C (Fig. 8iv). We will discuss possible explanations for the observed diversity of data from different techniques in detail below.

In addition, T-binned $n_{s,BET}(T)$ and $n_{s,geo}(T)$ spectra averaged in the log space are presented in Fig. S3. Similarly, we also present T-binned ratios of the individual measurements to the log fit of the data [All (log), Sus (log) or Dry (log) from Table 3] across the temperature range covered for all the measurement techniques (−37 °C < T < −11 °C) in Figs. S4–S8. These figures provide intercomparisons of the n_s deviations across the various techniques employed in this study.

4.2 Limitations of instrument types

Groups participating in this study used different experimental setups to measure immersion freezing efficiencies of illite NX test samples. As a consequence, various experimental procedures, such as particle generation, particle size-segregation, S_{total} estimation, ice crystal detection or counting, ice crystal detection size limits for OPCs or CCDs, and particle loss at the inlet and/or in the chamber can potentially yield substantial systematic uncertainties in the estimation of n_s. Below we qualitatively discuss potential errors and limitations involved in each instrument-type (cold stage, levitator, CECC and CFDC).

Limitations of substrate-supported optical microscopy and cold stage experimental setups may come from inhomogeneous cooling of the substrate and the surrounding media, the effects of RH changes surrounding the drops for non-substrate-supported cold stage setups, potential contamination during sample preparation and measurements (e.g., particle processing in a solvent) and/or uncontrollable heat transfer between the cold plate surface and the particle substrate (e.g., FRIDGE).

Levitator techniques require extensive pre-characterization of physicochemical properties. Furthermore, since the overall system characterization is more complex and labor intensive, only specific subsets (i.e., suspended samples or reference particles) can be examined using this method.

The development of AIDA-CECC allows the simulation of atmospherically representative cloud parcel formation and evolution (Möhler et al., 2003). Therefore, it is an advantage of CECC that the parameterization derived from its experiments can be most readily extended to atmospheric conditions (Niemand et al., 2012). Development of large (up to 84 m^3, i.e., AIDA) and/or temperature-controlled dynamic cloud simulation chambers (e.g., MRI-DCECC; Tajiri et al., 2013, a design which follows from DeMott

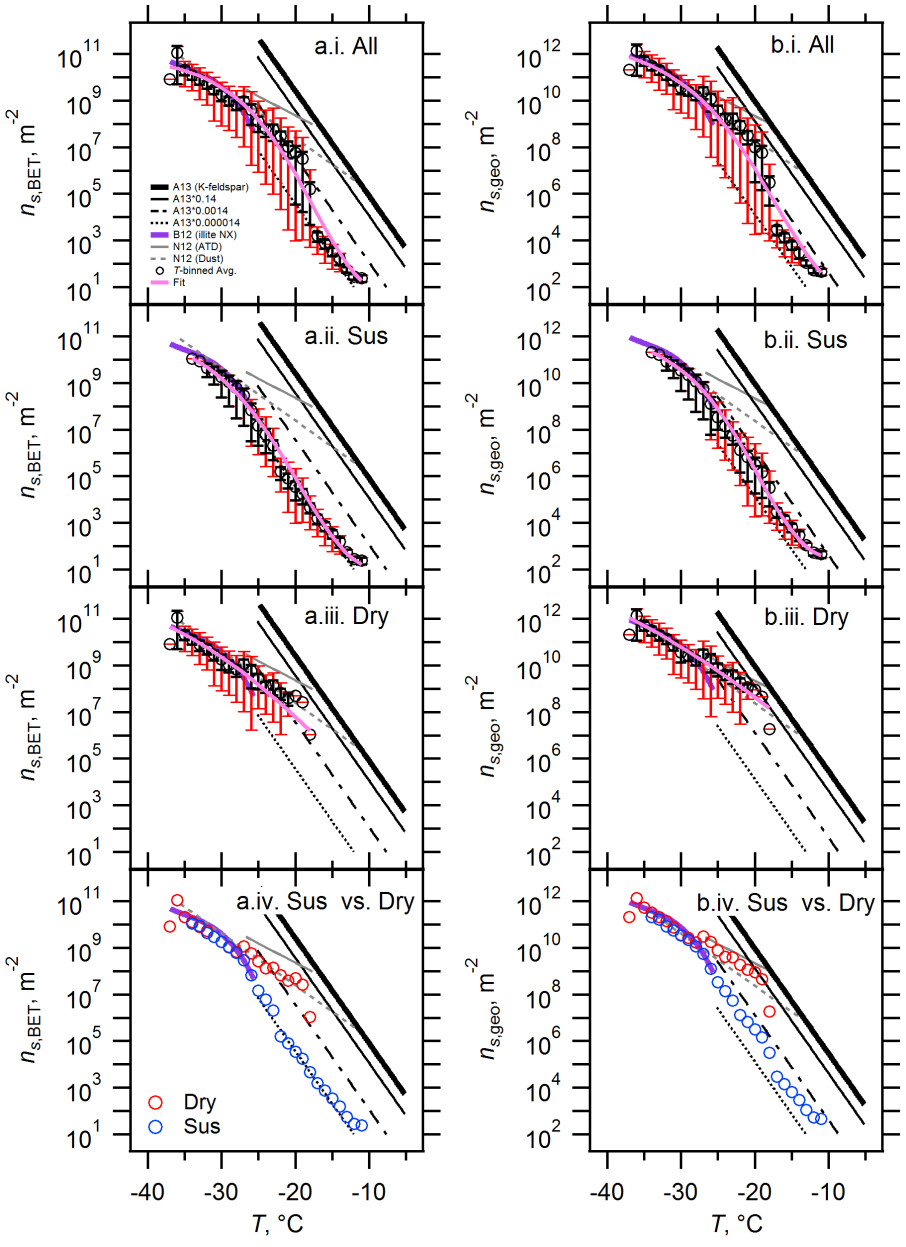

Figure 8. T-binned $n_{s,geo}$ **(a)** and $n_{s,BET}$ **(b)**. T-binned data (i.e., average in the linear space with 1 °C bins for $-37\,°C < T < -11\,°C$) of $n_s(T)$ spectra are presented for (i) All interpolated data set (All), (ii) suspension measurements (Sus), (iii) dry-dispersed particle measurements (Dry), and (iv) comparison between Sus and Dry. Red sticks represent maxima (positive direction) and minima (negative direction) and black sticks represent ±standard error. Literature results (B12, A13, and N12) are also shown.

and Rogers, 1990) enabled the exploration of heterogeneous ice nucleation properties of typical particulate samples in a wide range of particle concentrations, temperatures ($-100\,°C < T < 0\,°C$), cooling rates and nucleation times. However, the utilization of such an instrument to correctly measure the totality of INPs with a reasonable detection sensitivity ($< 0.1\,L^{-1}$), both in the lab and field settings, has not yet been realized due to CECC's limitations. These limitations include ice losses by settling (e.g., DeMott and Rogers, 1990) over the relatively long expansion periods in the confined vessel and internal turbulence during the expansion leading to heterogeneously supersaturated water vapor and temperature fields. These artifacts can bias IN measurements.

CFDCs are the most widely used technique to measure INPs in the atmosphere, but their inability to quantify INPs at high temperatures is an issue that exists due to the physical principals of operation, the limited sample volume (typically 1 to 2 L min^{-1}) and background frost formation in the

chamber over periods of operation. Based on the operational equations in Rogers (1988), the warmest operating temperature of a CFDC is approximately −6.5 °C, controlled by the fact that the warmest wall cannot exceed 0 °C. Low sample volumes necessitate integration over longer sample periods and result in a general lower detection limit of $0.2\,L^{-1}$ of sampled air, absent any particle pre-concentration (Prenni et al., 2009). According to Tobo et al. (2013), the highest temperature that can be achieved in a CFDC is −9 °C. Above this threshold, temperature and ice saturation conditions cannot be maintained in the chamber. Rogers et al. (2001) and other papers since have identified measurement issues due to frost emanating from the walls of the chamber when the dew point temperature of the sample air is not effectively controlled, although this appears to be an operational issue that can be mitigated if monitored properly, and will be most obtrusive for atmospheric sampling scenarios.

4.3 Stochastic nature of freezing and time dependence

The longstanding discussion of the stochastic theory (i.e., the freezing process is time-dependent) vs. the deterministic approximation (i.e., freezing occurs at specific temperature and humidity conditions) of heterogeneous freezing has introduced another complication towards complete understanding of heterogeneous ice nucleation in the atmosphere (Vali, 2014). Many studies have attempted to characterize ice nucleation based on the classical nucleation theory (CNT), which incorporates a nucleation rate (Murray et al., 2012; Kashchiev, 2000; Mullin, 2001). In this treatment, the ice nucleation process is always of a stochastic nature (i.e., time-dependent; Bigg, 1953; Vali, 1994, 2014). According to the nucleation rate approach, the heterogeneous ice nucleation rate is strongly sensitive to INP size and the kinetic activation energy of the ice embryo on the nucleating site/surface at a specific temperature (Khvorostyanov and Curry, 2000; Fletcher, 1962). A few variants of the CNT-based approaches have been developed over the past few decades. These approaches assume uniform surface characteristics and only one ice nucleation probability (i.e., a single contact angle), nominally categorized as the single component nucleation rate approach (e.g., Bigg, 1953). Several recent studies have applied a probability density function (PDF) of contact angles and active sites over the INP surface in CNT, or in other words described a distribution of nucleation efficiencies, bridging the gap between the stochastic theory and the deterministic treatment (Marcolli et al., 2007; Lüönd et al., 2010; Kulkarni et al., 2012; Niedemeier et al., 2011; Wright and Petters., 2013; Broadley et al., 2012).

The deterministic or time-independent singular approximation has been developed as an alternative option to quantitatively understand atmospheric ice nucleation. The concept was first developed by Levine (1950), while the term "active sites" per surface area was introduced by Fletcher (1969). More recently, Connolly et al. (2009) introduced the n_s density parameterization (see Sect. 2.4). This specific approach neglects the time dependence of freezing, and assumes that a characteristic condition (e.g., temperature) must be met to nucleate ice. The semi-deterministic forms of the singular approach have a cooling rate dependence incorporated (Vali, 2008; Herbert et al., 2014). Predicting ice nucleation from a singular perspective does not require a vast knowledge of particle-specific parameters (e.g., surface composition, structures, surface tension and solubility) that are particular to each ice nucleus and, therefore, enables ice nucleation parameterization to be relatively simple and efficient compared to the CNT-based approaches (Murray et al., 2011).

The assumption that the time dependence of the freezing of droplets is of secondary importance when compared to temperature dependence is supported by a recent modeling sensitivity study that shows that common INPs are substantially more sensitive to temperature than to time (Ervens and Feingold, 2013). Furthermore, while Broadley et al. (2012) shows that freezing by illite NX is time-dependent through isothermal experiments, the shift in freezing temperature on changing cooling rates by an order of magnitude is less than 0.6 °C, which is within the experimental uncertainty. A similar observation of weak time dependence of immersion freezing for various types of suspended samples, inferred by comparing the results with varied cooling rates from 0.01 to $1\,°C\,min^{-1}$, is reported by Wright et al. (2013).

In the context of dry-dispersed measurements, the sensitivity of the ice nucleation to a possible time dependence, and the respective influence on n_s, was examined to further discern its importance and uncertainty. Specifically, a contact angle distribution was fitted to the LACIS measurements and was used, together with the soccer ball model (SBM; Niedermeier et al., 2011, 2014), to simulate frozen fractions for different residence times varying over 4 orders of magnitude (i.e., 1, 10, 100 and 1000 s residence time). These frozen fractions were then used to calculate n_s, shown as lines in Fig. 9. More specifically, frozen fractions for 500 nm diameter illite NX particles were calculated based on SBM to obtain $n_s(T)$ spectra. To accomplish this, a contact angle distribution was used which was derived based on LACIS data for the illite NX particles as shown in this work, resulting in values of 1.90 rad for the mean and 0.27 rad for the width of the contact angle distribution. Frozen fractions were obtained for ice nucleation residence times of 1, 10, 100 and 1000 s. An increase in the residence time by a factor of 10 resulted in a shift of approximately 1 °C towards higher freezing temperatures. This is similar to the results found in a previous study by Welti et al. (2012) for measurements of kaolinite-rich clay minerals. Indeed, $n_{s,geo}$ data obtained from AIDA agree within the measurement uncertainty with LACIS data without accounting for time dependence. These results suggest that time dependence of immersion freezing for illite NX particles can be neglected as a factor in the comparisons shown in Figs. 4, 5 and 6. They also imply that the immersion freezing nature of illite NX is only slightly dependent on

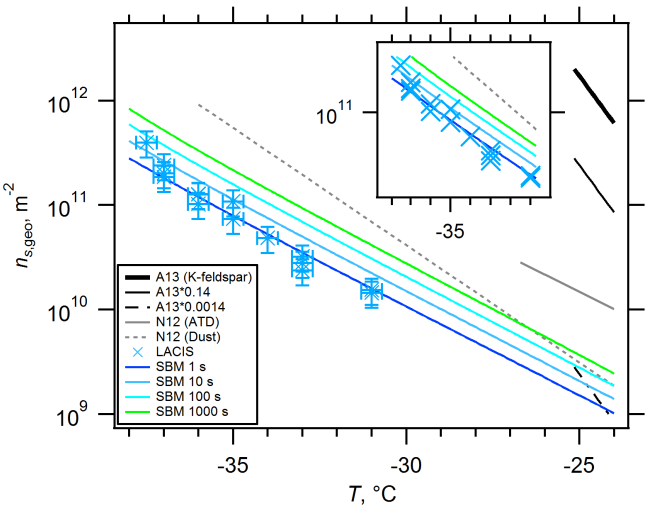

Figure 9. Soccer ball model analysis for time dependency of immersion freezing of illite NX particles. Comparison to LACIS measurements in $n_{s,geo}$ space is also shown. Error bars represent experimental uncertainties ($T \pm 0.3\,°C$ and $n_s \pm 28\,\%$). The subpanel shows a section of T (-31 to $-38\,°C$) and $n_{s,geo}$ (1.2×10^{10} to $5.1 \times 10^{11}\,m^{-2}$) space without error bars. A shift in the residence time from 1s to 10 s shifts n_s (as well as n_m, not shown) towards higher temperatures by about 1 °C.

cooling rate across a wider range of temperatures (as compared to a -26 to $-37\,°C$ range as shown in Broadley et al., 2012), regardless of the sample preparation process.

4.4 Potential effect of agglomerates

As seen in the particle surface area distributions (Fig. 2) and agglomerated-fractions based on a relative comparison to D_{95}, aggregates are rather persistent and dominant for most of the dry-dispersed particle measurements. Since dry aggregates can have large "supermicron" sizes, they may have different IN propensities and efficiencies (Wheeler et al., 2014) as compared to the smaller sizes investigated in the present study (i.e., up to 1000 nm from PINC). Further, the degree of agglomeration may conceivably affect the surface area exposed to liquid water when suspended in supercooled droplets. Hence, an overall quantification of the effect of agglomerates is difficult. Moreover, the degree of agglomeration seems to vary from experiment to experiment, introducing diversity on the estimation of S_{total} of particles and n_s for dry-dispersed particle measurements. For instance, a combination of several methods for particle dispersion and subsequent particle size selection was employed for particle generation from illite NX samples. Further, most of the dry dispersion techniques used upstream impactors to filter out large agglomerated particles and avoid counting these large particles as INPs. The different types of dispersion methods, impactors and size segregating instruments used in the present work are listed in the Supplement Table S1. These different aerosol generation processes may have caused different degrees of agglomeration. This may in part explain why n_s measurements obtained using dry dispersion techniques deviated from those using suspension measurements. Further quantification of the influences of different methods for particle dispersion, size-segregation and particle impaction/filtration on the estimation of S_{total} and n_s is an important topic for future works.

In contrast, in suspension experiments, illite NX samples were directly suspended in water. Despite no pre-treatments (e.g., pre-impaction or size segregation), suspended particles appeared adequately de-agglomerated (Fig. 2a). Though the number of immersed particles can vary from droplet to droplet and the random placement of particles in the drop may have an effect on the n_s values, the n_s spectra from suspension measurements are in reasonable agreement with slight deviations even over a wide range of wt % of illite NX samples (Figs. 6, 8, S4–S8). Thus, the influence of the random placement of particles in the drop and agglomeration on the n_s estimation for suspension measurements seems small. To support this, Wright and Petters (2013) and Hader et al. (2014) simulated the role of a statistical distribution in drops. The authors demonstrated that the random component due to drop placement seemed to be small relative to the statistical variation due to nucleation probability. Hence, assuming the degree of agglomeration or flocculation is similar in all suspension samples, the degree of agglomeration and the random placement of particles in the drop may lead to less pronounced deviations in n_s when compared to dry-dispersed measurements.

4.5 Nucleation mode dependence

While all suspension methods only measured immersion mode freezing of the illite NX particles, a contribution of other nucleation or freezing modes cannot be ruled out for dry-dispersed particle measurements. Hence, we now discuss inferences in the present experiments regarding the mode dependency of the ice nucleation ability of illite NX particles. Figure 10a and b show the comparison of n_s derived from the two different operation types of FRIDGE measurements. For instance, 'default mode' considers deposition mode nucleation and immersion mode freezing of dry particles in which RH_w is scanned upwards and 'imm.mode' counts immersion freezing of suspended particles in which the particles are first washed into droplets and then placed on the substrate. With these two different operational modes, FRIDGE investigated the ice nucleation ability of both dry and droplet suspended particles deposited on a substrate (see the supplementary methods). FRIDGE scans RH_{ice} and RH_w (low to high) at a constant temperature. During such scans an abrupt increase in an activated ice fraction near water saturation as well as the highest N_{ice} is typically observed. We consider ice crystals formed at the highest RH_w (near 100 % RH_w) as a measure of immersion N_{ice} from dry-dispersed

particle measurements in this study. Some default runs of FRIDGE show much higher $n_{s,BET}$ values compared to the immersion mode runs. This difference may be a consequence of the different IN efficiencies of nucleation modes (deposition + immersion vs. immersion alone) in the examined temperature range ($-25\,°C < T < -18\,°C$), the different sample preparation processes (dry or suspended sample), effects of agglomeration or a combination of the three. We note that a major difference between the two measurement setups is the pressure within the instrument. For instance, default conditions involve processing at a few hPa of water vapor while the immersion measurements are conducted at atmospheric pressure. In addition, corrective post-analysis of droplet/ice separation was taken into account in this study, so that errors from counting large droplets as ice crystals were successfully removed. Interestingly, our comparison suggests that n_s values derived from the FRIDGE default mode seem similar to those from MRI-DCECC, in which experiments were carried out with a high degree of particle agglomeration (Fig. 2c).

Some other variations on applied methods suggest nucleation mode effects on the IN efficiency of illite NX particles at lower temperatures (Fig. 10c and d). For instance, the comparison between ZINC and IMCA-ZINC show about an order of magnitude diversity in $n_{s,BET}$ beyond experimental uncertainties at $-33\,°C$, suggesting a mode-dependent IN efficiency of clay minerals at this temperature. This observation is consistent with a statement that the immersion freezing parameterization from CNT may not reliably predict the activated fraction observed at $RH_w > 100\,\%$ as observed from condensation freezing (Welti et al., 2014). However, this is in contrast to observations indicated by PNNL-CIC below $-25\,°C$ and to results presented in Wex et al. (2014), where $n_{s,geo}$ obtained from kaolinite measurements made with LACIS and the CSU-CFDC (at $104\,\% > RH_w > 106\,\%$ for the latter) agreed well. When a freezing point depression is taken into account, even data obtained with the CSU-CFDC for water-vapor-sub-saturated conditions is in agreement with data obtained from both LACIS and CSU-CFDC at water-vapor super-saturated conditions. Concerning data presented here, PNNL-CIC and IMCA-ZINC measure condensation/immersion and purely immersion mode freezing efficiency of particles, respectively, and are in reasonable agreement within experimental uncertainties (Fig. 10c and d). Thus, the observed inconsistencies between methods should be subject to further methodological improvements to provide accurate data as a basis for model parameterization. Similar heterogeneous ice nucleation mode-dependent observations were made by our EDB experiments. We observed that n_s values derived from contact freezing experiments were higher than those derived from immersion experiments (Fig. 10c and d). As described in the supplementary methods, immersion mode experiments were performed for the droplets, which were not activated via contact freezing.

4.6 Effect of mineralogical properties: which component of illite NX nucleates ice?

Atkinson et al. (2013) suggested that the mass fraction of K-feldspar in a sample can be used as a scaling factor to estimate the n_s values of other K-feldspar containing dust and soil samples. O'Sullivan et al. (2014) showed that this scaling rule could be used as an approximate predictor for the n_s of soil samples once the biological ice-nucleating particles were deactivated. However, inspection of Fig. 6 reveals that the line based on 14 % feldspar (assuming all microcline) significantly over predicts the n_s values for illite NX. There are a number of reasons why this might be.

The K-feldspar sample used by Atkinson et al. (2013) was the British Chemical Standard Chemical Reference Material (BCS-CRM) number 376/1 and X-ray diffraction analysis shows that the crystal structure is consistent with that of microcline. Microcline is one possible form of a K-feldspar and, as discussed above, other feldspars are sanidine and orthoclase, which have distinct crystal structures. The ice nucleation abilities of sanidine and orthoclase are not yet published, but given that they have different crystal structures, they may have different nucleating abilities. Unfortunately, the X-ray diffraction analysis of illite NX is unable to identify the K-feldspar(s) present in illite NX, although the mineralogical analysis conducted as part of this study concluded that there was no detectable microcline in illite NX. Hence, one explanation for the K-feldspar scaling rule not working for illite NX is that there is only a trace of the strongly ice active microcline present in illite NX. For suspension measurements, only the 0.0014 % microcline parameterization reproduces the slope and magnitude of the illite NX data in Fig. 6, but this quantity of microcline is well below the detection limit of the X-ray diffraction technique. Perhaps, in the case of illite NX, it may not be the feldspar which triggers nucleation, but instead it could be another mineral present in this sample. For example, Atkinson et al. (2013) found that a quartz sample nucleated ice more efficiently than the clay minerals, but less efficiently than the feldspar samples they used. At about $-28\,°C$, they reported an n_s of $\sim 10^{10}\,m^{-2}$. The X-ray analysis in this study revealed the presence of 3 % quartz, hence we would predict an n_s of $3 \times 10^8\,m^{-2}$, which is consistent with the illite NX data. Finally, an alternative explanation is that the surfaces of K-feldspars are chemically altered in illite NX. The surfaces of feldspars are known to transform to an amorphous silicate which can then recrystallize as a clay if exposed to an acidic environment. Wex et al. (2014) suggested that it was the acid processing of K-feldspar which deactivated Fluka-kaolinite. It is feasible that the surfaces of feldspar grains in illite NX have at some point become deactivated. More quantitative investigations of the acid processing of both reference and atmospherically relevant materials, and of acid processing's influence on their respective immersion mode ice nucleation efficiencies, are needed.

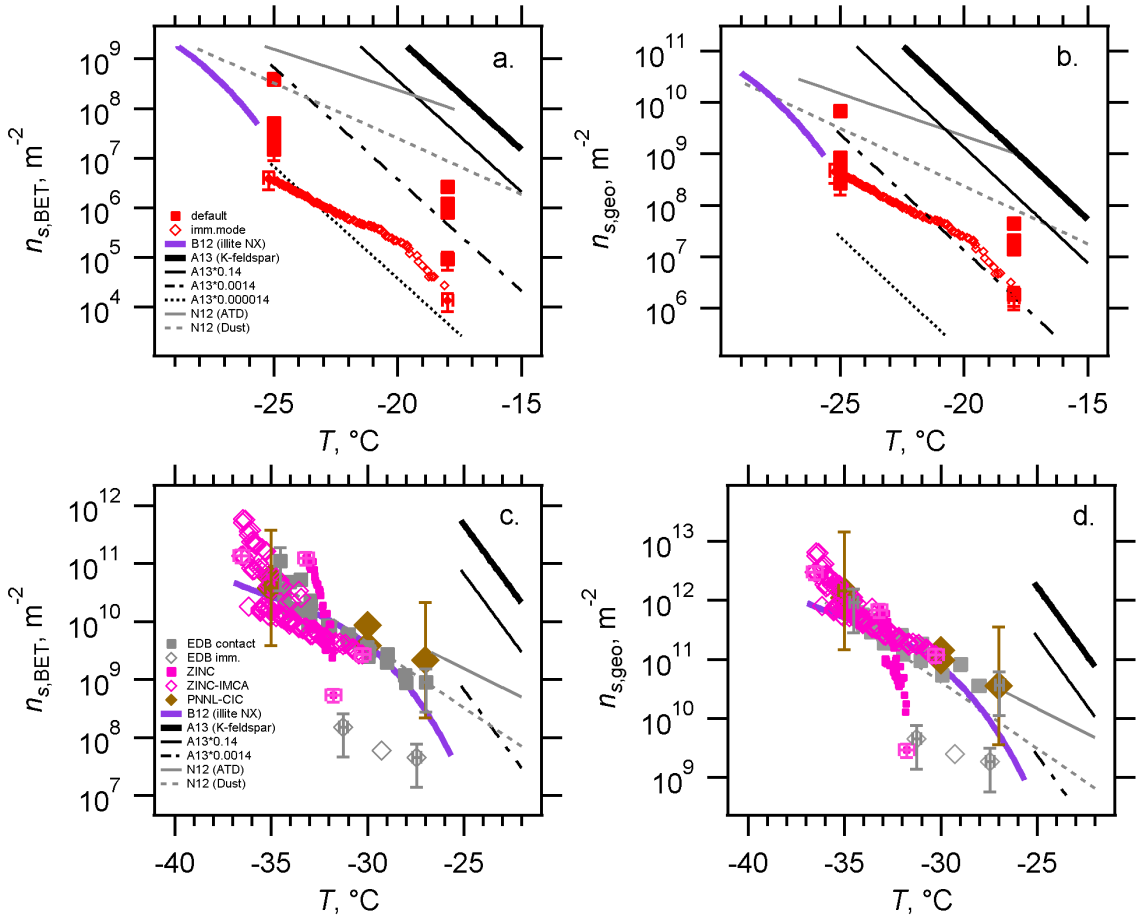

Figure 10. Examination of mode dependency of heterogeneous ice nucleation of illite NX particles. A comparison of FRIDGE (default) and FRIDGE (imm.mode) in $n_{s,BET}$ and $n_{s,geo}$ are shown in **(a)** and **(b)**, respectively. **(c)** and **(d)** show a comparison between EDB (contact), EDB (imm.), ZINC, IMCA-ZINC, and PNNL-CIC data in $n_{s,BET}$ and $n_{s,geo}$, respectively.

Recently, re-partitioning of soluble components of both swelling and non-swelling clay minerals and their effect on cloud condensation nucleation activity was reported (Sullivan et al., 2010; Kumar et al., 2011; Garimella et al., 2014). To address a potential importance of this effect on the ice-nucleating activity of illite NX in the wet dispersion experiments, we have measured the concentration of cations released by the illite NX sample placed into deionized water as a function of time, as described in Sect. 3.1 (i.e., Fig. 3).

It is instructive to compare the quantity of cations released by illite NX into an aqueous environment with the value of the cation exchange capacity (CEC) for illite, which is known to be 25 to 40 cmol kg^{-1}(Meunier and Velde, 2004). CEC is defined as the amount of cations retained by all the negative charges in 100 g of clay immersed in water at pH 7 (e.g., see Meunier, 2005). Per this definition, CEC describes the total quantity of exchangeable cations, including interlayer cations which are in fact not accessible for substitution in non-swelling clays. The molar fraction of external cations, located on the basal planes of the crystals and on the crystal edges is roughly evaluated for illites as 20 % of the total CEC, yielding 5 to 8 cmol kg^{-1} (Wilson, 2013). Remarkably, the total amount of all cations (K^+, Mg^{2+} and Ca^{2+}) released within the first hour by illite NX, if recalculated with account for cation valence and for the actual mass of illite in the aqueous suspension (0.1 g), gives the number 7.5 cmol kg^{-1}, which corresponds nicely with the upper bound of the external CEC (8 cmol kg^{-1}). Furthermore, Grim (1953) has shown that the CEC of illite increases with decreasing size of the clay particle size, with the upper bound ($\sim$ 40 cmol kg^{-1}) being characteristic for illite with a particle size below 100 nm. This is again consistent with the very small size of particles in illite NX.

These findings have two potential implications for the measurements of illite NX ice-nucleating efficiency obtained with different instruments. First, in the methods where dry illite NX particles are activated to droplets prior to cooling, the concentration of cations released into the water surrounding the particles is still far from the equilibrium and is a function of the residence time (e.g., $\sim$ 2–3 s for LACIS, $\sim$ 4 s for

PINC, ∼ 12 s for PNNL-CIC, and over the range of several tens of seconds to a few minutes for AIDA depending on initial chamber T and RH). At the same time, the amount of external cations retained on the surface of illite particles determines the charge properties, such as charge distribution landscape and zero charge point. A potential importance of the surface charge of hematite particles for their IN activity was suggested recently in Hiranuma et al. (2014b). These considerations, however speculative, might shed some light on the observed scattering of experimentally measured values of n_s. Second, for the freezing measurements where the illite-rich sample was suspended in water prior to cooling, all accessible external cations were already released into the aqueous environment. In these cases the concentration of cations in the droplets is a function of mass concentration of illite in suspension. To access high freezing temperatures, high concentrations of illite are needed in the droplet assay techniques, resulting in the possibility that not all cations are released into solution due to the inhibition of the ion exchange process. Again, this would change the surface charge distribution and potentially affect the ice-nucleating efficiency of illite particles. If wet particle generation (dispersion of aqueous suspension by means of a pressurized air atomizer) is used, the redistribution of cations between suspended particles may be an issue, as suggested by Garimella et al. (2014) for the case of CCN experiments. Further studies of samples without modification or ageing after dry dispersion or wet suspension are needed to get a better idea of the method intercomparison.

5 Conclusions

The framework of the present work is designed to advance the existing state of knowledge regarding IN measurement techniques. After ICIS-2007, there has been an increase in new instrument development, especially off-line, substrate-supported cold stage techniques, and modifications of existing online techniques. Concepts to formulate area-scaled IN efficiency with n_s parameters have also since been introduced to the community. These improvements are comprehensively evaluated in this work.

The partners of the INUIT group and external partners have for the first time identified and shared a reference mineral dust sample (illite NX) in order to obtain a comprehensive data set for evaluating immersion freezing properties of atmospherically relevant particles across a wide range of particle concentrations, temperatures, cooling rates and nucleation times. Illite NX samples were extensively characterized for their physicochemical properties before they were distributed to INUIT partners and collaborators. Both bulk and single particle elemental composition analyses were conducted by XRD and EDX analyses, respectively.

A total of 17 IN measurement techniques were intercompared based on their immersion freezing measurements. Our intercomparison exercise provided unique results that would not have been achieved by individual investigators in isolation. Both consistencies and discrepancies among the instruments have been identified. Our results suggest that the immersion freezing efficiency (i.e., n_s) of illite-rich clay minerals is relatively independent of droplet size, mass percent of illite NX sample in droplets for the methods examining suspensions, physical size of illite NX particles for the methods examining dry-dispersed particles and cooling rate during freezing within typical experimental uncertainties, verifying the premise of the n_s concept (i.e., size independency for submicron illite NX particles, strong temperature dependency and weak time dependency of immersion freezing for illite-rich clay mineral particles).

Furthermore, comparisons of the suspension subsets against the dry-dispersed particle techniques were performed. Dry samples alone showed higher n_s values compared to the pre-suspended samples above −27 °C. A possible explanation for this deviation (i.e., n_s from dry-dispersed methods > n_s from suspension methods) may be the surface modification of the illite NX particles (e.g., due to ion dissolution effects in the aqueous suspension).

Comparisons of the absolute values of $\Delta\log(n_s)/\Delta T$ as an ice activation parameter suggest that the predominant freezing sites of illite NX particles exist in a temperature range between −20 and −27 °C for suspension experiments. In comparison to previous measurements, our synergetic work, which covers a wide temperature range, shows a similar result to the Broadley parameterization (B12), and our overall fit for the low temperature region below −27 °C also agrees with the Niemand parameterization (N12).

Overall accuracy and precision of the IN measurement techniques was examined by evaluating T-binned (i.e., 1 °C bins) $n_s(T)$ data derived from all 17 instruments for the temperature range from −11 to −37 °C. Our analysis revealed that discrepancies among measurements were within about 8 °C in terms of temperature and up to 3 orders of magnitude with respect to n_s. This diversity is much larger than the individual uncertainties of each instrument, suggesting that all instruments may be reasonably precise but it is still difficult to find overall accuracy of current IN measurement techniques, at least while using illite NX as the standard and allowing partners to investigate it independently. In addition, two different n_s metrics, $n_{s,geo}$ and $n_{s,BET}$, were compared, and we found that $n_{s,BET}$ is a better proxy for suspension-based IN measurements, while $n_{s,geo}$ is better for dry-dispersed particle measurements.

Other than the intercomparison aspects described above, several important implications were inferred from our study and enhanced our basic knowledge of immersion freezing. First, the existence of only a comparably small contribution of time dependence to the intercomparison was reconciled by the SBM simulation. Specifically, a change of the residence time, from 1 to 10 s, shifts n_s values towards higher temperatures by only about 1 °C. Second, several

nucleation modes and their contribution to nucleation efficiency were also evaluated. A comparison among EDB, ZINC and IMCA-ZINC below −25 °C implied some mode dependencies. Likewise, a mode dependency was also pronounced based on FRIDGE results at temperatures above −25 °C. Third, immersion freezing experiments were performed with both polydisperse and size-selected illite NX particles for the AIDA-CECC, MRI-DCECC and CSU-IS measurements, and size independence of n_s for immersion freezing of submicron illite NX particles (DMA size-selected 200, 300 and 500 nm diameter) was also demonstrated. Finally, our observations show that temperature is the major variable influencing the immersion freezing of illite NX particles, as the n_s values in general increase while temperature decreases. In addition, our results of n_s and absolute values of $\Delta\log(n_s)/\Delta T$ distributions across a wide range of temperatures imply that clay minerals may contain various freezing activation energies, and the immersion freezing nature of clay minerals (e.g., illite NX) in a wide range of temperatures cannot be fitted by simple exponential functions but are governed by a hybrid of multi-exponential functions (a combination of scaled A13 and N12 parameterizations).

Though we shared identical test samples with each other, it is still difficult to compare n_s results because sample preparation techniques and measurement methods (e.g., particle dispersion and size distribution characterization) differ from group to group, which can result in different degrees of agglomeration or different nucleation modes. Therefore, a continued investigation to obtain further insights into consistencies or diversity of IN measurement techniques from an experimental perspective is important to explore freezing conditions for specific compositions and more atmospherically relevant particles (e.g., soil dusts and long range transported weathered dusts). In parallel, an empirically constrained model including parameterizations of immersion freezing that correctly and efficiently represent particle-specific experimental data is also in high demand for overall predictions of current and future climate. We demonstrated that the n_s formulation offers a simplified expression for quantitatively parameterizing immersion freezing. Further developments of more simplified (efficient but accurate) descriptions, constrained by more accurate IN counting techniques, of governing atmospheric IN processes are needed.

The Supplement related to this article is available online at doi:10.5194/acp-15-2489-2015-supplement.

Author contributions. J. Curtius and O. Möhler proposed the framework of this collaborative multi-institutional laboratory work. The overall manuscript, coordinated and led by N. Hiranuma, was a collaborative effort of the partners of the INUIT group and external partners. C. Budke and T. Koop designed and conducted the BINARY experiments, analyzed the data, and contributed the BINARY text. T. C. J. Hill carried out the CSU-IS measurements, analyzed the data, and contributed to the CSU-IS text. B. J. Murray, D. O'Sullivan and T. F. Whale performed the Leeds-NIPI experiments, analyzed the data, and contributed to the Leeds-NIPI text. K. Diehl performed the experiments and data analysis of M-AL and W-WT, and K. Diehl also contributed to their method summary text. J. D. Hader performed the NC State-CS experiments and analyzed the data, T. P. Wright contributed the analysis software, M. D. Petters designed the experiments, and J. D. Hader and M. D. Petters contributed to the NC State-CS text. G. P. Schill and M. A. Tolbert conducted the CU-RMCS experiments, analyzed the data, and contributed to the CU-RMCS text. N. Hiranuma and O. Möhler conceived the AIDA experiments, analyzed and discussed the results and contributed to the AIDA text. P. J. DeMott, E. J. T. Levin and C. S. McCluskey performed CSU-CFDC experiments, analyzed the data, and contributed to the CSU-CFDC text. N. Hoffmann and A. Kiselev carried out the EDB measurements with input on experimental techniques from T. Leisner and SEM measurements and contributed to the associated data analysis and text. Björn Nillius and Fabian Frank performed the FINCH experiments and analyzed the data, and D. Rose contributed to the FINCH uncertainty analysis and method summary text. A. Danielczok and H. Bingemer conducted the FRIDGE experiments, analyzed the data, and contributed to the FRIDGE text. S. Augustin-Bauditz did the LACIS experiments, D. Niedermeier derived contact angle distributions with SBM, and H. Wex performed SBM calculations and contributed to the LACIS text. M. Murakami, K. Yamashita, T. Tajiri and A. Saito designed and performed the MRI-DCECC experiments with assistance and contributions from N. Hiranuma and O. Möhler, K. Yamashita and N. Hiranuma analyzed the MRI-DCECC data, and K. Yamashita contributed to the method summary text. Z. A. Kanji conducted the PINC experiments, Y. Boose analyzed the data, Y. Boose and Z. A. Kanji interpreted and discussed the PINC data, and contributed to the PINC text. G. Kulkarni carried out the PNNL-CIC measurements, analyzed the data, and contributed to the PNNL-CIC text. A. Welti performed the IMCA-ZINC experiments, analyzed the data, and A. Welti and Z. A. Kanji contributed to the supplementary text. XRD measurements and analysis of illite NX were conducted by M. Ebert, K. Kandler and S. Weinbruch, and M. Ebert contributed the XRD text. IC measurements and analysis were carried out by A. Peckhaus and A. Kiselev, and A. Kiselev contributed to the IC text. DLS measurements and analysis were performed by K. Dreischmeier, and K. Dreischmeier also contributed to the DLS text. N. Hiranuma interpreted and analyzed the compiled data and wrote the paper. A. Kiselev and B. J. Murray co-wrote Sect. 4.6 with N. Hiranuma. All authors discussed the results and contributed to the final version of the manuscript.

Acknowledgements. Part of this work is funded by Deutsche Forschungsgemeinschaft (DFG) under contracts BU 1432/4-1, DI 1539/1-1, KO2944/2-1, MO668/4-1 and WE 4722/1-1 within Research Unit FOR 1525 (INUIT). The authors acknowledge partial financial support by Deutsche Forschungsgemeinschaft and Open Access Publishing Fund of Karlsruhe Institute of Technology. The authors gratefully acknowledge skillful and continuous support from their technical teams. G. Kulkarni acknowledges support from the Department of Energy (DOE) Atmospheric System Research

Program and thanks J. Fast for useful discussion. Battelle Memorial Institute operates the Pacific Northwest National Laboratory for DOE under contract DE-AC05-76RLO 1830. Z. A. Kanji acknowledges funding from Swiss National Funds. P. J. DeMott and T. Hill were funded by NSF grant award number AGS-1358495. M. A. Tolbert and G. P. Schill were funded by NSF Grant AGS 1048536. The MRI-DCECC work was partly funded by JSPS KAKENHI Grant Numbers 23244095. T. P. Wright, J. D. Hader, and M. D. Petters were funded by NSF Grant AGS 1010851. B. J. Murray, D. O'Sullivan and T. F. Whale acknowledge the Natural Environment Research Council (NE/K004417/1; NE/I020059/1; NE/I013466/1; NE/I019057/1) and The European Research Council (240449 – ICE) for funding. D. Niedermeier acknowledges financial support from the Alexander von Humboldt-foundation, Germany.

T. C. J. Hill would like to thank E. Levin and C. McCluskey for generation of size-selected particles. K. Diehl would like to thank S. K. Mitra for technical support on M-AL and M-WT and fruitful discussions. A. Kiselev and A. Peckhaus acknowledge O. Dombrowski for her support in IC measurements. N. Hiranuma thanks C. Anquetil-Deck for useful discussion. N. Hiranuma and G. Kulkarni thank T. Kisely and R. Ahmad for the N_2 BET and H_2O BET measurements, respectively. M. Ebert acknowledges R. Petschik for the additional high precision XRD measurements. N. Hiranuma and O. Möhler gratefully acknowledge technical support from M. Koyro and F. Schwartz for setting up the database for storing and updating the INUIT laboratory results. N. Hiranuma also thanks the AIDA technical team, including R. Buschbacher, T. Chudy, O. Dombrowski, E. Kranz, G. Scheurig and S. Vogt, for their professional support for the chamber maintenance and operation.

The article processing charges for this open-access publication have been covered by a Research Centre of the Helmholtz Association.

Edited by: D. J. Cziczo

References

Ardon-Dryer, K., Levin, Z., and Lawson, R. P.: Characteristics of immersion freezing nuclei at the South Pole station in Antarctica, Atmos. Chem. Phys., 11, 4015–4024, doi:10.5194/acp-11-4015-2011, 2011.

Atkinson, J. D., Murray, B. J., Woodhouse, M. T., Carslaw, K., Whale, T. F., Baustian, K., Dobbie, S., O'Sullivan, D., and Malkin, T. L.: The importance of feldspar for ice nucleation by mineral dust in mixed-phase clouds, Nature, 498, 355–358, doi:10.1038/nature12278, 2013.

Augustin-Bauditz, S., Wex, H., Kanter, S., Ebert, M., Stolz, F., Prager, A., Niedermeier, D., and Stratmann, F.: The immersion mode ice nucleation behavior of mineral dusts: A comparison of different pure and surface modifed dusts, Geophys. Res. Lett., 41, 7375–7382, doi:10.1002/2014GL061317, 2014.

Bickmore, B. R., Nagy, K. L., Sandlin, P., and Crater, T. S.: Quantifying surface areas of clays by atomic force microscopy, Am. Mineral., 87, 780–783, 2002.

Bigg, E. K.: The supercooling of water, Proc. Phys. Soc. B, 66, 688–694, doi:10.1088/0370-1301/66/8/309, 1953.

Bigg, E. K.: A new technique for counting ice-forming nuclei in aerosols. Tellus, 9: 394–400, doi:10.1111/j.2153-3490.1957.tb01895.x, 1957.

Bingemer, H., Klein, H., Ebert, M., Haunold, W., Bundke, U., Herrmann, T., Kandler, K., Müller-Ebert, D., Weinbruch, S., Judt, A., Wéber, A., Nillius, B., Ardon-Dryer, K., Levin, Z., and Curtius, J.: Atmospheric ice nuclei in the Eyjafjallajökull volcanic ash plume, Atmos. Chem. Phys., 12, 857–867, doi:10.5194/acp-12-857-2012, 2012.

Boucher, O., Randall, D., Artaxo, P., Bretherton, C., Feingold, G., Forster, P., Kerminen, V.-M., Kondo, Y., Liao, H., Lohmann, U., Rasch, P., Satheesh, S. K., Sherwood, S., Stevens, B., and Zhang, X. Y.: Clouds and Aerosols, in: Climate Change 2013: The Physical Science Basis. Contribution of Working Group I to the Fifth Assessment Report of the Intergovernmental Panel on Climate Change, edited by: Stocker, T. F., Qin, D., Plattner, G.-K., Tignor, M., Allen, S. K., Boschung, J., Nauels, A., Xia, Y., Bex, V., and Midgley, P. M., Cambridge University Press, Cambridge, United Kingdom and New York, NY, USA, 571–657, 2013.

Broadley, S. L., Murray, B. J., Herbert, R. J., Atkinson, J. D., Dobbie, S., Malkin, T. L., Condliffe, E., and Neve, L.: Immersion mode heterogeneous ice nucleation by an illite rich powder representative of atmospheric mineral dust, Atmos. Chem. Phys., 12, 287–307, doi:10.5194/acp-12-287-2012, 2012.

Brunauer, S., Emmett, P. H., and Teller, E.: Adsorption of gases in multimolecular layers, J. Am. Chem. Soc., 60, 309–319, doi:10.1021/ja01269a023, 1938.

Budke, C. and Koop, T.: BINARY: an optical freezing array for assessing temperature and time dependence of heterogeneous ice nucleation, Atmos. Meas. Tech., 8, 689–703, doi:10.5194/amt-8-689-2015, 2015.

Bundke, U., Nillius, B., Jaenicke, R., Wetter, T., Klein, H., and Bingemer, H.: The fast ice nucleus chamber FINCH, Atmos. Res., 90, 180–186, doi:10.1016/j.atmosres.2008.02.008, 2008.

Chou, C., Stetzer, O., Weingartner, E., Jurányi, Z., Kanji, Z. A., and Lohmann, U.: Ice nuclei properties within a Saharan dust event at the Jungfraujoch in the Swiss Alps, Atmos. Chem. Phys., 11, 4725–4738, doi:10.5194/acp-11-4725-2011, 2011.

Christenson, H.: Two-step crystal nucleation via capillary condensation, Cryst. Eng. Comm., 15, 2030–2039, doi:10.1039/C3CE26887J, 2013.

Connolly, P. J., Möhler, O., Field, P. R., Saathoff, H., Burgess, R., Choularton, T., and Gallagher, M.: Studies of heterogeneous freezing by three different desert dust samples, Atmos. Chem. Phys., 9, 2805–2824, doi:10.5194/acp-9-2805-2009, 2009.

Cwilong, B. M.: Sublimation centers in a Wilson chamber, Proc. Roy. Soc. A, 190, 137–143, doi:10.1098/rspa.1947.0066, 1947.

DeMott, P. J. and Rogers, D. C.: Freezing nucleation rates of dilute solution droplets measured between $-30°$ and $-40\,°C$ in laboratory simulations of natural clouds. J. Atmos. Sci., 47, 1056–1064, doi:10.1175/1520-0469(1990)047<1056:FNRODS>2.0.CO;2, 1990.

DeMott, P. J.: Quantitative descriptions of ice formation mechanisms of silver iodide-type aerosols, Atmos. Res., 38, 63–99, doi:10.1016/0169-8095(94)00088-U, 1995.

DeMott, P. J., Möhler, O., Stetzer, O., Vali, G., Levin, Z., Petters, M. D., Murakami, M., Leisner, T., Bundke, U., Klein,

H., Kanji, Z. A., Cotton, R., Jones, H., Benz, S., Brinkmann, M., Rzesanke, D., Saathoff, H., Nicolet, M., Saito, A., Nillius, B., Bingemer, H., Abbatt, J., Ardon, K., Ganor, E., Georgakopoulos, D. G., and Saunders, C.: Resurgence in ice nuclei measurement research, B. Am. Meteorol. Soc., 92, 1623–1635, doi:10.1175/2011BAMS3119.1, 2011.

DeMott, P. J., Prenni, A. J., McMeeking, G. R., Sullivan, R. C., Petters, M. D., Tobo, Y., Niemand, M., Möhler, O., Snider, J. R., Wang, Z., and Kreidenweis, S. M.: Integrating laboratory and field data to quantify the immersion freezing ice nucleation activity of mineral dust particles, Atmos. Chem. Phys., 15, 393–409, doi:10.5194/acp-15-393-2015, 2015.

Diehl, K., Mitra, S. K., Szakáll, M., Blohn, N. v., Borrmann, S., and Pruppacher, H. R.: Chapter 2. Wind Tunnels: Aerodynamics, Models, and Experiments, in: The Mainz Vertical Wind Tunnel Facility: A Review of 25 Years of Laboratory Experiments on Cloud Physics and Chemistry, edited by: Pereira, J. D., Nova Science Publishers, Inc., Hauppauge, NY, USA, 2011.

Diehl, K., Debertshäuser, M., Eppers, O., Schmithüsen, H., Mitra, S. K., and Borrmann, S.: Particle surface area dependence of mineral dust in immersion freezing mode: investigations with freely suspended drops in an acoustic levitator and a vertical wind tunnel, Atmos. Chem. Phys., 14, 12343–12355, doi:10.5194/acp-14-12343-2014, 2014.

Durant, A. J. and Shaw, R. A.: Evaporation freezing by contact nucleation inside-out, Geophys. Res. Lett., 32, L20814, doi:10.1029/2005GL024175, 2005.

Dymarska, M., Murray, B. J., Sun, L. M., Eastwood, M. L., Knopf, D. A., and Bertram, A. K.: Deposition ice nucleation on soot at temperatures relevant for the lower troposphere, J. Geophys. Res., 111, D04204, doi:10.1029/2005JD006627, 2006.

Ervens, B. and Feingold, G.: Sensitivities of immersion freezing: Reconciling classical nucleation theory and deterministic expressions, Geophys. Res. Lett., 40, 3320–3324, doi:10.1002/grl.50580, 2013.

Fletcher, N. H.: Physics of Rain Clouds, Cambridge Univ. Press, New York, NY, USA, 386 pp., 1962.

Fletcher, N. H.: Active sites and ice crystal nucleation, J. Atmos. Sci., 26, 1266–1271, doi:10.1175/1520-0469(1969)026<1266:ASAICN>2.0.CO;2, 1969.

Fornea, A. P., Brooks, S. D., Dooley, J. B., and Saha, A. Heterogeneous freezing of ice on atmospheric aerosols containing ash, soot, and soil, J. Geophys. Res., 114, D13201, doi:10.1029/2009JD011958, 2009.

Fournier D'albe, E. M.: Some experiments on the condensation of water vapour at temperatures below 0° C, Q. J. Roy. Meteorol. Soc., 75, 1–16, doi:10.1002/qj.49707532302, 1949.

Friedman, B., Kulkarni, G., Beránek, J., Zelenyuk, A., Thornton, J. A., and Cziczo, D. J.: Ice nucleation and droplet formation by bare and coated soot particles, J. Geophys. Res., 116, D17203, doi:10.1029/2011JD015999, 2011.

Friedrich, F., Steudel, A., and Weidler, P. G.: Change of the refractive index of illite particles by reduction of the Fe content of the octahedral sheet, Clays Clay Miner., 56, 505–510, doi:10.1346/CCMN.2008.0560503, 2008.

Garimella, S., Huang, Y.-W., Seewald, J. S., and Cziczo, D. J.: Cloud condensation nucleus activity comparison of dry- and wet-generated mineral dust aerosol: the significance of soluble material, Atmos. Chem. Phys., 14, 6003–6019, doi:10.5194/acp-14-6003-2014, 2014.

Gregg, S. L. and Sing, K. S. W.: Adsorption, Surface Area and Porosity, Academic Press, London, UK, 303 pp., 1982.

Grim, R. E.: Clay mineralogy, McGraw-Hill, New York, USA, 384 pp., 1953.

Hader, J. D., Wright, T. P., and Petters, M. D.: Contribution of pollen to atmospheric ice nuclei concentrations, Atmos. Chem. Phys., 14, 5433–5449, doi:10.5194/acp-14-5433-2014, 2014.

Hartmann, S., Niedermeier, D., Voigtländer, J., Clauss, T., Shaw, R. A., Wex, H., Kiselev, A., and Stratmann, F.: Homogeneous and heterogeneous ice nucleation at LACIS: operating principle and theoretical studies, Atmos. Chem. Phys., 11, 1753–1767, doi:10.5194/acp-11-1753-2011, 2011.

Herbert, R. J., Murray, B. J., Whale, T. F., Dobbie, S. J., and Atkinson, J. D.: Representing time-dependent freezing behaviour in immersion mode ice nucleation, Atmos. Chem. Phys., 14, 8501–8520, doi:10.5194/acp-14-8501-2014, 2014.

Hill, T. C. J., Moffett, B. F., DeMott, P. J., Georgakopoulos, D. G., Stump, W. L., and Franc, G. D.: Measurement of Ice Nucleation-Active Bacteria on Plants and in Precipitation by Quantitative PCR, Appl. Environ. Microbiol., 80, 1256–1267, doi:10.1128/AEM.02967-13, 2014.

Hiranuma, N., Brooks, S. D., Moffet, R., Glen, A., Laskin, A., Gilles, M. K., Liu, P., MacDonald, M. A., Strapp, W., and McFarquhar, G. M.: Chemical characterization of individual particles and residuals of cloud droplets and ice crystals collected on board research aircraft in the ISDAC 2008 study, J. Geophys. Res., 118, 6564–6579, doi:10.1002/jgrd.50484, 2013.

Hiranuma, N., Paukert, M., Steinke, I., Zhang, K., Kulkarni, G., Hoose, C., Schnaiter, M., Saathoff, H., and Möhler, O.: A comprehensive parameterization of heterogeneous ice nucleation of dust surrogate: laboratory study with hematite particles and its application to atmospheric models, Atmos. Chem. Phys., 14, 13145–13158, doi:10.5194/acp-14-13145-2014, 2014a.

Hiranuma, N., Hoffmann, N., Kiselev, A., Dreyer, A., Zhang, K., Kulkarni, G., Koop, T., and Möhler, O.: Influence of surface morphology on the immersion mode ice nucleation efficiency of hematite particles, Atmos. Chem. Phys., 14, 2315–2324, doi:10.5194/acp-14-2315-2014, 2014b.

Hoffmann, N., Kiselev, A., Rzesanke, D., Duft, D., and Leisner, T.: Experimental quantification of contact freezing in an electrodynamic balance, Atmos. Meas. Tech., 6, 2373–2382, doi:10.5194/amt-6-2373-2013, 2013.

Hoose, C., Kristjansson, J. E., Chen, J.-P., and Hazra, A.: A classical-theory-based parameterization of heterogeneous ice nucleation by mineral dust, soot, and biological particles in a global climate model, J. Atmos. Sci., 67, 2483–2503, doi:10.1175/2010JAS3425.1, 2010.

Hoose, C. and Möhler, O.: Heterogeneous ice nucleation on atmospheric aerosols: a review of results from laboratory experiments, Atmos. Chem. Phys., 12, 9817–9854, doi:10.5194/acp-12-9817-2012, 2012.

Hussain, K. and Saunders, C. P. R.: Ice nucleus measurement with a continuous flow chamber. Q. J. Roy. Meteorol. Soc., 110, 75–84, doi:10.1002/qj.49711046307, 1984.

Iannone, R., Chernoff, D. I., Pringle, A., Martin, S. T., and Bertram, A. K.: The ice nucleation ability of one of the most abundant

types of fungal spores found in the atmosphere, Atmos. Chem. Phys., 11, 1191–1201, doi:10.5194/acp-11-1191-2011, 2011.

Kanji, Z. A. and Abbatt, J. P. D.: Laboratory studies of ice formation via deposition mode nucleation onto mineral dust and n-hexane soot samples, J. Geophys. Res., 111, D16204, doi:10.1029/2005JD006766, 2006.

Kanji, Z. A. and Abbatt, J. P. D.: The University of Toronto Continuous Flow Diffusion Chamber (UT-CFDC): A simple design for ice nucleation studies, Aerosol Sci. Technol., 43, 730–738. doi:10.1080/02786820902889861, 2009.

Kanji, Z. A., Welti, A., Chou, C., Stetzer, O., and Lohmann, U.: Laboratory studies of immersion and deposition mode ice nucleation of ozone aged mineral dust particles, Atmos. Chem. Phys., 13, 9097–9118, doi:10.5194/acp-13-9097-2013, 2013.

Kashchiev, D.: Nucleation: Basic Theory with Applications, Butterworth-Heinemann, Oxford, UK, 544 pp., 2000.

Khvorostyanov, V. I. and Curry, J. A.: A new theory of heterogeneous nucleation for application in cloud and climate models, Geophys. Res. Lett., 27, 4081–4084, doi:10.1029/1999GL011211, 2000.

Kline, D. B. and Brier, G. W.: Some experiments on the measurement of natural ice nuclei, Mon. Weather Rev., 89, 263–272, doi:10.1175/1520-0493(1961)089<0263:SEOTMO>2.0.CO;2, 1961.

Knopf, D. A. and Alpert, P. A.: A water activity based model of heterogeneous ice nucleation kinetics for freezing of water and aqueous solution droplets, Faraday Discuss., 165, 513–534, doi:10.1039/C3FD00035D, 2013.

Koehler, K. A., Kreidenweis, S. M., DeMott, P. J., Petters, M. D., Prenni, A. J., and Möhler, O.: Laboratory investigations of the impact of mineral dust aerosol on cold cloud formation, Atmos. Chem. Phys., 10, 11955–11968, doi:10.5194/acp-10-11955-2010, 2010.

Koop, T., Luo, B., Tsias, A., and Peter, T.: Water activity as the determinant for homogeneous ice nucleation in aqueous solutions, Nature, 406, 611–614, doi:10.1038/35020537, 2000.

Kulkarni, G., Fan, J., Comstock, J. M., Liu, X., and Ovchinnikov, M.: Laboratory measurements and model sensitivity studies of dust deposition ice nucleation, Atmos. Chem. Phys., 12, 7295–7308, doi:10.5194/acp-12-7295-2012, 2012.

Kumar, P., Sokolik, I. N., and Nenes, A.: Cloud condensation nuclei activity and droplet activation kinetics of wet processed regional dust samples and minerals, Atmos. Chem. Phys., 11, 8661–8676, doi:10.5194/acp-11-8661-2011, 2011.

Levine, J.: Statistical Explanation of Spontaneous Freezing of Water Droplets, NACA Tech. Notes, no. 2234, 1950.

Lüönd, F., Stetzer, O., Welti, A., and Lohmann, U.: Experimental study on the ice nucleation ability of size-selected kaolinite particles in the immersion mode, J. Geophys. Res., 115, D14201, doi:10.1029/2009JD012959, 2010.

Marcolli, C., Gedamke, S., Peter, T., and Zobrist, B.: Efficiency of immersion mode ice nucleation on surrogates of mineral dust, Atmos. Chem. Phys., 7, 5081–5091, doi:10.5194/acp-7-5081-2007, 2007.

Marcolli, C.: Deposition nucleation viewed as homogeneous or immersion freezing in pores and cavities, Atmos. Chem. Phys., 14, 2071–2104, doi:10.5194/acp-14-2071-2014, 2014.

Meunier, A.: Clays, Springer, 472 pp., Berlin, Heidelberg, Germany, 2005.

Meunier, A. and Velde, B. D.: Illite: Origins, Evolution and Metamorphism, Springer, 286 pp., Berlin, Heidelberg, Germany, 2004.

Möhler, O., Stetzer, O., Schaefers, S., Linke, C., Schnaiter, M., Tiede, R., Saathoff, H., Krämer, M., Mangold, A., Budz, P., Zink, P., Schreiner, J., Mauersberger, K., Haag, W., Kärcher, B., and Schurath, U.: Experimental investigation of homogeneous freezing of sulphuric acid particles in the aerosol chamber AIDA, Atmos. Chem. Phys., 3, 211–223, doi:10.5194/acp-3-211-2003, 2003.

Mullin, J. W.: Crystallization, Elsevier Butterworth-Heinemann, Oxford, UK, Forth edn., 600 pp, 2001.

Murray, B. J., Broadley, S. L., Wilson, T. W., Bull, S. J., Wills, R. H., Christenson, H. K., and Murray, E. J.: Kinetics of the homogeneous freezing of water, Phys. Chem. Chem. Phys., 12, 10380–10387, doi:10.1039/c003297b, 2010.

Murray, B. J., Broadley, S. L., Wilson, T. W., Atkinson, J. D., and Wills, R. H.: Heterogeneous freezing of water droplets containing kaolinite particles, Atmos. Chem. Phys., 11, 4191–4207, doi:10.5194/acp-11-4191-2011, 2011.

Murray, B. J., O'Sullivan, D., Atkinson, J. D., and Webb, M. E.: Ice nucleation by particles immersed in supercooled cloud droplets, Chem. Soc. Rev., 41, 6519–6554, doi:10.1039/c2cs35200a, 2012.

Niedermeier, D., Shaw, R. A., Hartmann, S., Wex, H., Clauss, T., Voigtländer, J., and Stratmann, F.: Heterogeneous ice nucleation: exploring the transition from stochastic to singular freezing behavior, Atmos. Chem. Phys., 11, 8767–8775, doi:10.5194/acp-11-8767-2011, 2011.

Niedermeier, D., Ervens, B., Clauss, T., Voigtländer, J., Wex, H., Hartmann, S., and Stratmann, F.: A computationally efficient description of heterogeneous freezing: A simplified version of the soccer ball model, Geophys. Res. Lett., 41, 736–741, doi:10.1002/2013GL058684, 2014.

Niehaus, J, Bunker, K. W., China, S., Kostinski, A., Mazzoleni, C., and Cantrell, W.: A technique to measure ice nuclei in the contact mode, J. Atmos. Oceanic Technol., 31, 913–922, doi:10.1175/JTECH-D-13-00156.1, 2014.

Niemand, M., Möhler, O., Vogel, B., Vogel, H., Hoose, C., Connolly, P., Klein, H., Bingemer, H., DeMott, P., and Skrotzki, J.: A particle-surface-area-based parameterization of immersion freezing on desert dust particles, J. Atmos. Sci., 69, 3077–3092, doi:10.1175/Jas-D-11-0249.1, 2012.

O'Sullivan, D., Murray, B. J., Malkin, T. L., Whale, T. F., Umo, N. S., Atkinson, J. D., Price, H. C., Baustian, K. J., Browse, J., and Webb, M. E.: Ice nucleation by fertile soil dusts: relative importance of mineral and biogenic components, Atmos. Chem. Phys., 14, 1853–1867, doi:10.5194/acp-14-1853-2014, 2014.

Palmer, H. P.: Natural ice-particle nuclei, Q. J. Roy. Meteorol. Soc., 75, 17–22, doi:10.1002/qj.49707532303, 1949.

Prenni, A. J., DeMott, P. J., Rogers, D. C., Kreidenweis, S. M., McFarquhar, G. M., Zhang, G., and Poellot, M. R.: Ice nuclei characteristics from M-PACE and their relation to ice formation in clouds, Tellus, 61B, 436–448, doi:10.1111/j.1600-0889.2009.00415.x, 2009.

Quantachrome Instruments: autosorb iQ/ASiQwin Operating Manual, Sect. J. Theory and Discussion, 359–360, 2013.

Riechers, B., Wittbracht, F., Hütten, A., and Koop, T.: The homogeneous ice nucleation rate of water droplets produced in a mi-

crofluidic device and the role of temperature uncertainty, Phys. Chem. Chem. Phys., 15, 5873–5887, doi:10.1039/c3cp42437e, 2013.

Rogers, D. C.: Development of a continuous flow thermal gradient diffusion chamber for ice nucleation studies, Atmos. Res., 22, 149–181, doi:10.1016/0169-8095(88)90005-1, 1988.

Rogers, D. C., DeMott, P. J., Kreidenweis, S. M., and Chen, Y.: A continuous-flow diffusion chamber for airborne measurements of ice nuclei, J. Atmos. Oceanic Technol., 18, 725–741, doi:10.1175/1520-0426(2001)018<0725:ACFDCF>2.0.CO;2, 2001.

Rosenfeld, D. and Woodley, W. L.: Deep convective clouds with sustained supercooled liquid water down to −37.5 °C, Nature, 405, 440–442, doi:10.1038/35013030, 2000.

Schill, G. P. and Tolbert, M. A.: Heterogeneous ice nucleation on phase-separated organic-sulfate particles: effect of liquid vs. glassy coatings, Atmos. Chem. Phys., 13, 4681–4695, doi:10.5194/acp-13-4681-2013, 2013.

Steinke, I., Möhler, O., Kiselev, A., Niemand, M., Saathoff, H., Schnaiter, M., Skrotzki, J., Hoose, C., and Leisner, T.: Ice nucleation properties of fine ash particles from the Eyjafjallajökull eruption in April 2010, Atmos. Chem. Phys., 11, 12945–12958, doi:10.5194/acp-11-12945-2011, 2011.

Stetzer, O., Baschek, B., Luond, F., and Lohmann, U.: The Zurich Ice Nucleation Chamber (ZINC) – A new instrument to investigate atmospheric ice formation, Aerosol Sci. Technol., 42, 64–74, doi:10.1080/02786820701787944, 2008.

Sullivan, R. C., Moore, M. J. K., Petters, M. D., Kreidenweis, S. M., Qafoku, O., Laskin, A., Roberts, G. C., and Prather, K. A.: Impact of particle generation method on the apparent hygroscopicity of insoluble mineral particles, Aerosol Sci. Tech., 44, 830–846, doi:10.1080/02786826.2010.497514, 2010.

Szakáll, M., Diehl, K., Mitra, S. K., and Borrmann, S.: A wind tunnel study on the shape, oscillation, and internal circulation of large raindrops with sizes between 2.5 and 7.5 mm, J. Atmos. Sci., 66, 755–765, doi:10.1175/2008JAS2777.1, 2009.

Tajiri, T., Yamashita, K., Murakami, M., Orikasa, N., Saito, A., Kusunoki, K., and Lilie, L.: A novel adiabatic-expansion-type cloud simulation chamber. J. Meteor. Soc. Japan, 91, 687–704, doi:10.2151/jmsj.2013-509, 2013.

Tobo, Y., Prenni, A. J., DeMott, P. J., Huffman, J. A., McCluskey, C. S. , Tian,G., Pöhlker,C., Pöschl, U., and Kreidenweis, S. M.: Biological aerosol particles as a key determinant of ice nuclei populations in a forest ecosystem, J. Geophys. Res.-Atmos., 118, 10100–10110, doi:10.1002/jgrd.50801, 2013.

Tomlinson, E. M. and Fukuta, N.: A new horizontal gradient, continuous flow, ice thermal diffusion chamber. J. Atmos. Oceanic Technol., 2, 448–467, doi:10.1175/1520-0426(1985)002<0448:ANHGCF>2.0.CO;2., 1985.

Vali, G.: Nucleation terminology, J. Aerosol Sci., 16, 575–576, doi:10.1016/0021-8502(85)90009-6, 1985.

Vali, G.: Freezing rate due to heterogeneous nucleation, J. Atmos. Sci., 51, 1843–1856, doi:10.1175/1520-0469(1994)051<1843:FRDTHN>2.0.CO;2, 1994.

Vali, G.: Repeatability and randomness in heterogeneous freezing nucleation, Atmos. Chem. Phys., 8, 5017–5031, doi:10.5194/acp-8-5017-2008, 2008.

Vali, G.: Interpretation of freezing nucleation experiments: singular and stochastic; sites and surfaces, Atmos. Chem. Phys., 14, 5271–5294, doi:10.5194/acp-14-5271-2014, 2014.

Veghte, D. P. and Freedman, M. A.: Facile method for determining the aspect ratios of mineral dust aerosol by electron microscopy, Aerosol Sci. Technol., 48, 715–724, doi:10.1080/02786826.2014.920484, 2014.

Wagner, R., Möhler, O., Saathoff, H., Schnaiter, M., and Leisner, T.: New cloud chamber experiments on the heterogeneous ice nucleation ability of oxalic acid in the immersion mode, Atmos. Chem. Phys., 11, 2083–2110, doi:10.5194/acp-11-2083-2011, 2011.

Waseda, Y., Matsubara, E., and Shinoda, K.: X-Ray Diffraction Crystallography: Introduction, Examples and Solved Problems, Springer, 310 pp., Berlin, Heidelberg, Germany, 2011.

Wegener, A.: Thermodynamik der Atmosphäre, J. A. Barth Verlag, 331 pp., Leipzig, Germany, 1911.

Welti, A., Lüönd, F., Stetzer, O., and Lohmann, U.: Influence of particle size on the ice nucleating ability of mineral dusts, Atmos. Chem. Phys., 9, 6705–6715, doi:10.5194/acp-9-6705-2009, 2009.

Welti, A., Lüönd, F., Kanji, Z. A., Stetzer, O., and Lohmann, U.: Time dependence of immersion freezing: an experimental study on size selected kaolinite particles, Atmos. Chem. Phys., 12, 9893–9907, doi:10.5194/acp-12-9893-2012, 2012.

Welti, A., Kanji, Z. A., Lüönd, F., Stetzer, O., and Lohmann, U.: Exploring the mechanisms of ice nucleation on kaolinite: from deposition nucleation to condensation freezing, J. Atmos. Sci., 71, 16–36, doi:10.1175/JAS-D-12-0252.1, 2014.

Welton, J. E.: SEM Petrology Atlas, The American Association of Petroleum Geologists, Tulsa, OK, USA, 240 pp., 1984.

Wex, H., DeMott, P. J., Tobo, Y., Hartmann, S., Rösch, M., Clauss, T., Tomsche, L., Niedermeier, D., and Stratmann, F.: Kaolinite particles as ice nuclei: learning from the use of different kaolinite samples and different coatings, Atmos. Chem. Phys., 14, 5529–5546, doi:10.5194/acp-14-5529-2014, 2014.

Wheeler, M. J., Mason, R. H., Steunenberg, K., Wagstaff, M., Chou, C. and Bertram, A. K.: Immersion freezing of supermicron mineral dust particles: freezing results, testing different schemes for describing ice nucleation, and ice nucleation active site densities, J. Phys. Chem. A, Article ASAP, doi:10.1021/jp507875q, 2014.

Wilson, M. J.: Sheet Silicates: Clay Minerals, in: Rock-Forming Minerals, Volume 3C, edited by: Deer, W. A., Howie, R. A., and Zussman, J., The Geological Society, 736 pp., London, UK, 2013.

Wright, T. P. and Petters, M. D.: The role of time in heterogeneous freezing nucleation, J. Geophys. Res. Atmos., 118, 3731–3743, doi:10.1002/jgrd.50365, 2013.

Wright, T. P., Petters, M. D., Hader, J. D., Morton, T., and Holder, A. L.: Minimal cooling rate dependence of ice nuclei activity in the immersion mode, J. Geophys. Res.-Atmos., 118, 1–9, doi:10.1002/jgrd.50810, 2013.